Wingtip Vortex Structure in the Near-Field of Swept-Tapered Wings

S.N. Skinner*

Department of Aerospace Engineering,

University of Maryland, College Park, MD, 20742, USA

R.B. Green†, H. Zare-Behtash‡

Department of Aerospace Sciences, University of Glasgow, Scotland, G12 8QQ, UK

Abstract

Wingtip vortices are an important phenomenon in fluid dynamics due to their complex and negative impacts. Despite numerous studies, the current understanding of the inner vortex is very limited, thus a basis for the design of effective wingtip geometry and vortex manipulation is narrow. This work examines the structure of the trailing vortex shed from a swept-tapered wing; analogous to a commercial aircraft topology. Stereoscopic particle imaging velocimetry (sPIV) has been utilised to compare the vortex structure and development through several angles of attack at various downstream stations for a fixed Reynolds number ($Re = 1.5 \times 10^6$). After correcting for vortex meander, through helicity-based spatial localisation of the vortex core, relationships between the vortex core velocity/vorticity fields, core shape, and turbulent properties have been examined. Subsequently, the vortex is found to exhibit a layered structure with slow linear rates of dissipation indicative of laminar diffusion mechanisms: despite being a turbulent vortex. The turbulent kinetic energy distribution in the vortex signals that relaminarisation of the inner core occurs. Consideration of the streamline curvature around the core, via examination of the local Richardson number, indicated that a laminar core structure had formed within which large scale turbulent eddies could not contribute to the turbulent diffusion of vorticity away from the core. The normalised circulation within the vortex core has been shown to exhibit self-similar behaviour typical of fully developed axisymmetric vortices.

* Research Scientist, University of Maryland. Corresponding author: skinner1@umd.edu

† Senior Lecturer, University of Glasgow.

‡ Lecturer, University of Glasgow.

Nomenclature

b	=	Wing span
c	=	Local wing chord
$\overline{c}$	=	Mean aerodynamic chord
H_x	=	Streamwise helicity
k	=	Turbulent kinetic energy ($= \frac{1}{2}(\overline{u'^2} + \overline{v'^2} + \overline{w'^2})$
M_∞	=	Mach number
Re	=	Reynolds number ($= \frac{\rho_\infty U_\infty L}{\mu}$)
Ri	=	Richardson number ($= 2S_p(S_p + 1)$)
$r,\ \theta,\ x$	=	Cylindrical (polar) coordinates
r_c	=	Mean vortex core radius
S_p	=	Bradshaw non-dimensional shape parameter
U_∞	=	Freestream flow velocity
$u,\ v,\ w$	=	Axial, lateral, and vertical velocity components in Cartesian coordinates
$\overline{u'^2},\ \overline{v'^2},\ \overline{w'^2}$	=	Turbulent normal stresses in Cartesian coordinates
$u_r,\ u_\theta,\ u_x$	=	Radial, tangential (swirl), and axial velocity in cylindrical coordinates
$\overline{v'w'}$	=	In-plane Reynolds shear stresses ($= \overline{(v_i - \overline{v})(w_i - \overline{w})}$)
$x,\ y,\ z$	=	Dimensionless Cartesian coordinates
α	=	Angle of attack
Γ	=	Vortex circulation
Γ_c	=	Vortex core circulation
Δt	=	Laser pulse separation
δ^*	=	Boundary-layer displacement thickness
$\varepsilon_{yz} = \varepsilon_{zy}$	=	Shear strain
θ_v	=	Azimuthal coordinate
μ	=	Dynamic viscosity
ν	=	Kinematic viscosity
ρ	=	Density
ω_x	=	Streamwise vorticity

I. INTRODUCTION

The longitudinal vortex system generated by an aircraft's wings, due to the induced drag contribution and the hazardous effects on flight safety, continue to be of deep interest and concern to the aviation industry. One of the significant challenges is the problem of improving flight safety in the increasingly crowded airspace in the vicinity of airports[1,2]. The encounter of an aircraft during take-off or landing with the wake generated by a preceding aircraft can pose a serious hazard which is particularly dangerous as it occurs at low altitude. Loss of control and altitude, and strong structural loads, are some of the dangers that the following aircraft may suffer if subjected to the vortex wake of another aircraft; this interaction has led to the injury and deaths of passengers[3–6]. As a result, the International Civil Aviation Organisation (ICAO) regulate minimum separation standards between aircraft; this consequently leads to increased operational costs and airport congestion[2,7]. Thus, with projected increases in the demand for air transportation, with ever larger aircraft entering existing fleets (*e.g.* Boeing's 777x), it can be expected that this hazard will increase and be an impediment to future air traffic capacity[8].

In 2019, Airbus predicted global air traffic to double every year (from 2018) with the total number of operational passenger aircraft estimated to reach $45,265$ by 2037[9]. However, due to the 2020 COVID-19 pandemic, such predicted growth is now unclear due to both the potential long term impact of the pandemic on the aviation industry and/or global economic crisis depressing demand. However, analysts expect airlines to use the downturn for rapid modernisation - hastening the retirement of older fleets and maintaining planned deliveries of newer models[10]. In addition, business/private jet aviation may see an increased demand for transatlantic flights[11].

Nonetheless, future aircraft must comply with strategic research agendas developed by the Advisory Council for Aeronautics Research in Europe (ACARE) which aims to enforce strict emission targets by 2050 - CO_2 emissions per passenger kilometre to be reduced by 75%, NO_x emissions by 90% and perceived noise by 65%, all relative to the year 2000[8]. Similarly, the ICAO in conjunction with the Federal Aviation Administration (FAA) and the National Aeronautics and Space Administration (NASA) have goals to mature fuel efficient technologies by 2030 in order to meet the same targets as ACARE by 2050[12]. For new aircraft fleets to be designed in such a way as to radically reduce the wingtip vortex strength, and

consequently lift induced drag, perceived aircraft noise, and overall environmental impact, technological advances in the aircraft's passive wing aerodynamics must be leveraged to manipulate, alleviate, and/or control the wingtip vortex.

Trailing vortices can exhibit high tangential and axial velocities in the vicinity of the vortex core which vary with flight condition, wingspan, and wing loading. The trailing vortices can persist far downstream of the aircraft for hundreds of wingspans before they are dissipated due to instability mechanisms and/or atmospheric effects[2,13]. This means that for a typical transport/cargo aircraft (with either conventional planar wings, or wings with winglets), the trailing vortex system can have life spans of tens-of-minutes, and persist for downstream distances exceeding $30km$.

Substantial efforts have been made to develop theoretical and numerical models for the roll-up process of trailing wingtip vortices[14–31]. The bulk of experimental investigations, largely required for the investigation of vortex dynamics and numerical validation, have been either qualitative in nature or directed toward tracking the mean tangential/axial velocities of the trailing vortex as a function of downstream range. Such experimental campaigns[31–46] have primarily been restricted to wings of simple rectangular planform, conducted to investigate the dynamics of the tip vortex formation around the wingtip and its development as it propagates through the near-field. Considerably fewer in number, other investigations have examined the vortex system shed from platforms which are both swept and tapered and therefore more analogous to that of commercial aircraft[47–54]. Of these experimental studies, very little information is provided regarding the behaviour, structure, or development of the vortex core due to limitations in the spatiotemporal resolution available from the experimental diagnostics employed (*e.g.* five-hole pressure probes, low-resolution PIV). For this reason, there remains a need to improve the understanding of the initial establishment, growth, structure, and development of wingtip vortices from formation through to dissipation. An improved understanding in the near-field fluid dynamics of wingtip vortices will enlighten the design of future wingtip devices enabling the production of lower vorticity, rapid decay, vortex systems and provided validation data for numerical simulations.

This work concentrates on the near-field vortex wake characteristics of a planar wing arrangement at $Re = 1.5 \times 10^6$ (based on the wing's mean aerodynamic chord); the flow structure of the tip vortex has been examined using stereoscopic particle imaging velocimetry (sPIV), providing non-intrusive high spatial resolution vortex realizations at $200Hz$. This

investigation documents the wake vortex formation, analysing the evolution of the tangential and axial velocity distribution, the vortex core shape, the vorticity distribution, and the low frequency ($\leq 100Hz$) turbulent properties of the vortex core. Skinner and Zare-Behtash[55] have previously assessed the aerodynamic and aeroelastic behaviours of the wing which will be referred to throughout this work.

II. EXPERIMENTAL SET-UP

A. Semi-Span Wind Tunnel Model

The planar wing, shown in Figure 1, is analogous of a typical mid-sized transport commercial aircraft wing topology, representing a 10% scale model. Relevant wing specifications and scaling information is provided in Table 1. The fuselage, a generic axisymmetric half-body fairing, is mounted to an AMTI OR6-7 1000 series force platform located beneath the working section's floor; the electromechanical centre of the force platform, is aligned with the pitch axis of the model, the model's centre-of-gravity, and the model's aerodynamic centre (shown in Figure 1). The wing is untwisted with a constant NACA 63_1-412 aerofoil section. Due to lack of wing twist (washout) sub-optimal lift distribution over the wingspan is expected. The wing and fuselage sections are constructed from polyurethane foams with

TABLE 1: Wing parameters.

	Conventional full-scale	Semi-span model
Mach Number (M_∞)	$\approx$ 0.78-0.8	0.145
Reynolds Number (Re)	$\approx 10^8$-10^9	1.5×10^6
Altitude (h) $[m]$	$\approx$ 10972.8 $(36,000ft)$	0
Dynamic Pressure (q_∞) $[Pa]$	$\approx$ 10107.04	$\approx$ 1531.25
(Main) Wing Area (S) $[m^2]$	$\approx$ 65-90	0.5717
MAC ($\bar{c}$) $[m]$	$\approx$ 4-5	0.44
Wing Semi-Span ($b/2$) $[m]$	$\approx$ 17-19	1.50
Taper Ratio (λ)	$\approx$ 0.2	0.21
Aspect Ratio (AR)	$\approx$ 4-5	4.12
Wing Sweep ($\Lambda_{0.25c}$)	$\approx 25°$-$30°$	$30°$

an aerodynamically smooth finish of surface roughness $< 0.1\mu m$ (surface roughness grade $N3$).

Evident from Figure 1, the semi-span model does not utilise a transitional peniche extrusion at the model's symmetry plane cross section, and instead a stand-off gap is employed. Skinner and Zare-Behtash[56] showed that this has the advantage of preventing the development of a horseshoe vortex immediately upstream of the model, which would envelope the fuselage and deteriorate flow over the inboard wing. In this study, the stand-off gap is scaled to four times the wind tunnel wall boundary-layer displacement thickness (δ^*) at the pitch axis (located at the mounting shaft) of the model. Figure 1 additionally indicates that the position of the model's centre-of-gravity is aligned with the mounting shaft.

While not addressed in this study, Skinner and Zare-Behtash[55] and Skinner[57] provide information regarding the model's structural dynamics and investigate the aerodynamic performance of the wing which is not explicitly shown in this work, but is referred to. For the same range of conditions, this study aims to quantify the development of the trailing vortex system produced by the wing between $0° \leq \alpha \leq 14°$. For $\alpha \leq 8°$ the flow remains attached over the wing's surface; however, beyond this separation begins to develop at the wingtip.

B. Experimental Facility

The de Havilland National Wind Tunnel Facility (dH) is an atmospheric closed return wind tunnel circuit. The working section has an octagonal cross-section of $2.65m$ width, $2.04m$ height, and $5.64m$ length with a contraction ratio of 5:1. The corner fillets are arranged to enable the test section's cross-sectional area to expand from inlet to outlet compensating for boundary-layer growth and offset the resulting longitudinal static pressure gradients which contribute to horizontal buoyancy. For the experimental conditions presented here, the turbulence intensity along the centre line of the working section length is 0.4%. Further, detailed characterisation of the dH working section is provided elsewhere[57]. As mentioned, the semi-span model is mounted via a steel mounting shaft interface to a AMTI OR6-7 1000 series force platform. The force platform is housed within the working section's $2m$ diameter ATE AEROTECH turntable, which controls the model's angle of attack with a position accuracy of $\pm 0.005°$.

Stereoscopic particle imaging velocimetry (sPIV) has been used to provide instantaneous and time-averaged global flow field measurements of the near field trailing vortex. Over a range of angles of attack, sPIV planes used within this work are located at several distances aft of the wing's mean aerodynamic centre, scaled by the wing mean aerodynamic chord. For convenience these planes will be referred to: $x/\bar{c} = 1.35$, 1.5, 2.0, 2.5, and 5.418. Note, the model's longitudinal location of aerodynamic centre is aligned with its centre-of-gravity. Figure 2 shows experimental arrangement of the planar wing installed in the dH working section along with the sPIV set-up; a schematic of the sPIV planes relative to the model is also provided.

The sPIV system consisted of: two high-speed 4 Megapixel Phantom $v341$ cameras on Scheimpflug mounts, positioned on either side of the working section; imaging optics (Canon automatic focus lenses with $200mm$ focal lengths set at f 2.8) providing a 400×200 mm field of view; a pulsed laser (Litron double-cavity Nd:YAG laser, providing $100mJ$ pulse^{-1}); and olive oil tracer particles ($1\mu m$ in diameter) generated by a PIVtec-GmbH Aerosol Generator PivPart160 series device. The tracer particles were illuminated by a $4mm$ thick laser sheet, spanning the wind tunnel perpendicular to the freestream (shown in Figure 2). The light sheet arrangement was set up to accommodate the dominant out-of-plane tracer displacements, while providing sufficient illumination of particles to track in-plane tracer displacements over the laser separation pulse, Δt. The laser separation pulse/experimental arrangement was selected to resolve both the tangential (in-plane) and the axial (out-of-plane) velocity components; see Skinner[57] for further information. In this work, a pulse separation of $\Delta t = 25\mu s$ has been used with a data acquisition rate of $200Hz$. Optical access was provided through large optical grade glass windows on the port and starboard walls, as well as several optical access points on the roof of the working section (visible in Figure 2).

DaVis 8[58] was used for image capturing and image processing. Before performing stereo cross-correlation, the raw tracer images were pre-processed using a particle intensity normalisation (PIN) filter. This compensated for the fluctuations in seeding density inside of the vortex core due to high centrifugal forces, and facilitated an enhanced spatial accuracy within the vortex core. Figure 3(a) presents the instantaneous seeding distribution through the trailing vortex produced for $\alpha = 8°$ at plane $x/\bar{c} = 2.5$, as viewed from the starboard camera ('Camera 2' in Figure 2). A core diameter of $20mm$ is indicated ($\approx 4.5\%$ of the mean

aerodynamic chord); the dark region within the vortex core is approximately 75% ($15mm$) of the vortex core diameter. Figure 3(b) illustrates the effect of applying the PIN filter to the raw data. It is emphasized that applying this filter only manipulates the relative tracer signal, and not the tracer position. Consequently, a valid detection probability of at least 90% was achieved per interrogation window. In the current study, good quality seeding and imaging provide a high level of reliability to the experiments, and therefore no vector post-processing was necessary. The stereo cross-correlation of the image pairs, composed of a double step 32×32 pixel interrogation window with a 25% overlap, followed by a double step 16×16 pixel interrogation window with a 50% overlap. With this arrangement, two adjacent velocity vectors were separated by $1.002mm$ (median vortex diameter is $20mm$; 4.5% of the mean aerodynamic chord).

The calibration of the set up was carried out with a purpose-specific LaVision calibration plate aligned with the laser sheet (perpendicular to the flow), from which LaVision FlowMaster software was used to perform stereo three-dimensional pinhole calibration[58]. The resulting calibration error was < 0.3 pixels for all experiments with no trends/bias/gradient of the dewarped marker positions (*i.e.* uniform dewarping observed). Such a result is indicative of a well-conditioned experimental arrangement[58].

Measurements with an absolute error greater than $1/10^{th}$ of a pixel were marked as invalid with the intention of excluding them from statistical analysis. It is noted that no vectors in the vicinity of the vortex were identified to have an absolute error exceeding this - only vectors at the image edges were flagged. The instantaneous particle velocity has been taken to equal the instantaneous fluid velocity at the particle position, which is a valid approach for the majority of the flow field, where the flow timescales are smaller than the typical particle relaxation time (τ_p) of approximately $2.7\mu s$. Additionally, the Stokes number (St) is of the order 10^{-4} within the trailing vortex for all test cases; Raffel et al.[59] demonstrated that if a Stokes number of $St < 0.06$ could be achieved, then the root mean square tracing error can be assumed $< 1\%$. To assess the numerical errors arising from integration and interpolation, tracer particles were integrated one sample time-step backwards, and subsequently forwards, in time. Comparing the resulting position with the original position indicated a local error estimate below $10^{-4}U_\infty$.

III. SPATIAL LOCALISATION OF THE VORTEX CORE

Trailing wingtip vortices are non-stationary flows that exhibit small random motions normal to the vortex axis. This phenomenon is referred to as vortex meander (or wander). In practice, vortex meander produces a spreading effect in the time-averaged flow field measurement, which vary in both amplitude and frequency with time. This results in an artificial spreading/blurring effect producing a larger apparent vortex core size with diminished peak magnitudes of the vortex properties (e.g. tangential velocity, vorticity, etc.) compared to any instantaneous measurement. It is common practice to acknowledge the presence of vortex wander but assume that the effects, without quantification, are negligible[60]. Analysis of the effects of wandering is necessary to accurately reveal flow structures inside the core region, and to give confidence in the measurements made outside the core[35,61]. Whatever the source of the wandering (wing vibrations, freestream turbulence, etc.), the vortex core translation and its effect on vortex properties must be acknowledged.

The implementation of a methodology capable of extracting vortex wander information to spatially adjust instantaneous vector fields in the construction of the time-averaged vector field ensemble requires close consideration. The spatial centering of the instantaneous vortex realisations can be considered as a post-processing procedure in which the solid-body translations of the vortex and the turbulent fluctuations within the core are separated. Aligning the instantaneous realisations of the vortex, therefore localising their centres, assumes that wandering is only a function of the solid-body translations of the vortex on the plane perpendicular to its axis; radial deformations/fluctuations of the vortex are not considered. Thus, the challenge is to identify a robust methodology that can define and track instantaneous vortex core centres. There are two approaches available from the literature: 1) identification of the vortex centre by tracking flow field properties inside of the vortex core[62–64]; and 2) the application of a discrete mask to the data assuming the behaviour of an analytical vortex model[61,65]. The first approach is dependent upon the accuracy and spatial resolution of the experimental measurements within the vortex core, while the latter is dependent upon an appropriate least square fit over a range of variables (such as vortex centre position, velocity, orientation, core radius, and circulation) to a reasonable analytical model.

In the early wake ($x/\bar{c} \leq 10$[66]) the vortex may not be axisymmetric and/or show interactions with the wake sheet, these traits would be poorly described by analytical models. In

this work, it was found that while the wake sheet interacted with the trailing vortex, enough tracer particles were present within the vortex core, such that the sPIV measurements resulted in a sufficiently high vector spatial resolution (of $1mm$) and reliability to track flow properties within the core; resulting in approximately 20 vectors over the core diameter. Thus, in this study, the first approach is adopted for the identification and tracking of the instantaneous realisations of vortex core centres for spatial re-alignment.

Methods for detecting the vortex centre from sPIV measurements of the core can be based on several different properties of the vortex. Analytically, all of these methods would indicate the same location of the vortex core. Skinner[57] provides a detailed analysis of several tracking methods including: 1) tracking the centroid of the seeding void - due to centrifugal forces in the vortex core; 2) zero in-plane velocity (or swirl centre); 3) peak axial velocity perturbation; 4) peak vorticity; 5) peak helicity; 6) minimum Q-criterion; and 7) peak of the eigenvalues of the velocity gradient tensor, λ_2. The effects of each vortex centering method is discussed with particular attention paid to the tangential and axial velocity distributions, vorticity distributions, circulation profiles, and turbulent quantities.

Of the methods listed above, Skinner[57] demonstrated that tracking peak helicity of the vortex was the most robust methodology to achieve spatial localisation of the vortex core. Helicity is a conserved quantity which measures the helical motion of a vortex. It is defined as the dot product of the velocity and vorticity such that the result indicates the inclination between the vorticity vector and the velocity vector. In this work only the streamwise vorticity is available. As the wingtip vortex convects downstream with the freestream flow, an appropriate definition is the scalar product of the axial velocity perturbation and the vorticity is presented in equation 1[63]:

$$H_x = |u_x - U_\infty| \cdot \omega_x \tag{1}$$

where the streamwise component of vorticity is defined as:

$$\omega_x = \frac{\partial w}{\partial y} - \frac{\partial v}{\partial z} \tag{2}$$

In this work, the streamwise vorticity is calculated via the eight-node circulation method described by Raffel et al.[59] which is shown to perform better than other schemes in terms of error and smoothness of the results. This method can be employed due to the sufficiently high spatial resolution.

Correcting for the vortex wander is effectively a spatial filtering operation applied ahead of further post-processing, inherently dictating different vortex structures, whereby each should be closely scrutinized. For brevity, here we will only consider the effects of spatial localisation on the understanding of shear strain rate (a second-order term) within the trailing vortex core at $x/\bar{c} = 2.5$, and $\alpha = 8°$ over 1800 sample frames, shown in Figure 4. The shear strain rate, ε_{yz}, defined as:

$$\varepsilon_{yz} = \varepsilon_{zy} = \frac{1}{2}(\frac{\partial v}{\partial z} + \frac{\partial w}{\partial y}), \tag{3}$$

calculated utilising an eight-point scheme presented by Raffel et al.[59].

Figure 4 illustrates a four-lobed pattern, with alternating positive and negative components of shear strain rates - vortex shear strain rates will be discussed in Section VIII. The shear strain rates are observed to show the same four-lobed pattern outside of the vortex core independent of the averaging method used, with peak magnitudes varying by $< 10\%$ relative to the simple averaged case. The most distinct variations between centering methodology occur inside of the vortex core structure. Centering methods such as zero in-plane and peak axial perturbation velocity consider only the simplest mechanics of the vortex, and thus manipulate the vortex spatial realignment with narrow consideration - this is evident once higher order characteristics are considered. Considering the simple averaged case (Figure 4(a)), there is a distinct void of available information within the vortex core; note that the mean vortex core diameter is shown. The same is observed for the zero in-plane centering method, shown in Figure 4(b), although it is found to reduce the magnitude of the shear strains observed - it is highlighted that properties such as peak tangential velocity, core radius, and turbulent kinetic energy are found to improve. With the application of the helicity centering method, shown in Figure 4(c), a remarkable actualisation of information within the vortex core becomes available. The helicity, vorticity, and Q-criterion methods each revealed similar properties within the vortex core.

The helicity based correction method is the only method mentioned here which uses all available velocity components, and provides consistent description of the inner vortex core structure without bias to an individual property. The vorticity and Q-criterion methods have also proven reasonably robust with the exception of sufficiently describing inner core axial velocity perturbations. The Q-criterion (and the λ_2) centering method is complex, computationally expensive, and introduces errors from the calculation of the flow field gradients

while not providing any clear advantage. The zero in-plane and axial velocity perturbations cannot accurately account for the whole vortex structure, particularly when considering turbulence analysis. Hence, the helicity centering method will be used for correcting the vortex motions during data acquisition, having been found to be the most appropriate in describing the tangential and axial velocity distributions, vorticity profiles, and turbulent properties of the vortex core, including Reynolds stress and shear strain rates. Each of these methods and their relative performance has been discussed in detail by Skinner[57].

Subsequently, it is beneficial to briefly consider how the vortex meander amplitude varies (defined by the helicity tracking method) as a function of both wing angle of attack and downstream distance. Figure 5 shows the probability density functions (PDF) of the vortex meander amplitude for different angles of attack and downstream stations. Figure 5(a) suggests insensitivity of the wander amplitude to angle of attack; results for meander are presented in the $y/\bar{c}$ and $z/\bar{c}$ axes separately to illustrate the isotropic distribution. Such behaviour is observed at all downstream $x/\bar{c}$ planes. For any given angle of attack, the vortex meander increases with downstream convection away from the wing as shown in Figure 5(b). This suggests that the dominant source of meander is from wind tunnel freestream turbulence. Isotropic wander amplitudes are also observed with downstream translation (see Figure 5(b)).

Figure 6 presents the vortex meander amplitude spectra (up to $100Hz$) for the same data set shown in Figure 5. These spectra have been calculated using Welch's method[67]. In Figure 6, frequencies $7.2Hz$, $10.3Hz$, and $33.5Hz$ have been highlighted as these correspond to meaningful frequencies present within the experimental arrangement. The $7.2Hz$ and $33.5Hz$ correspond to the first and second bending modes of the wing, while the $10.3Hz$ corresponds to the rotational speed of the wind tunnel fan ($\approx$ 615 rpm)[55]. Figure 6(a) indicates that the vortex meander, as a function of the angle of attack, is influenced by the wing bending modes and the frequency of the wind tunnel fan. Greater sensitivity to these frequencies is found in the $y/\bar{c}$ axis (direction of wing lift and increased wing flexibility). We observe that for low angles of attack ($0° \leq \alpha \leq 2°$), there is a general indication of meandering frequency around $7Hz$ and $10Hz$. With the higher range of the lift-curve-slope ($4° \leq \alpha \leq 6°$), the observed spectra are generally quieter although a frequency peak near $10Hz$ can persist. At these angles of attack the wing is sufficiently loaded such that the wing's vibrations are attenuated[55]. For $\alpha > 8°$, we observe a broadening of spectral

frequencies over the range of $7Hz$ to $10Hz$, with post-stall angles of attack indicating a second spectral peak near $33.5Hz$. These effects are related to the buffeting motion of the wing. For all angles of attack it is noted that spectral peaks can intermittently appear around $5Hz$ and $15Hz$; the physical mechanism for this is unknown and it is acknowledged that they may be artifacts of the centering methodology.

Figure 6(b) shows how the trailing vortex at $\alpha = 8°$ meander frequencies evolve with downstream range. Close to the wing (at $x/\overline{c} = 1.35$) there are no distinct frequency peaks, although large amplitude-low frequency meandering is observed. Moving downstream, the influence of the wing's first bending mode can be seen to get stronger and broaden, eventually merging with the $10Hz$ range. No clear $33.5Hz$ peak is noticed - as mentioned, this frequency was only observed for higher angles of attack. At $x/\overline{c} = 5.418$, the vortex meander generally becomes nosier as higher frequency turbulence begins to play a more significant role.

Assessment of the statistical convergence and uncertainty for several vortex properties, with the application of the helicity based centering method, is presented in Appendix XI A. Based on this analysis all sPIV data presented has been averaged over 1800 samples to provide statistical convergence with a peak uncertainty of $< 4\%$ within the vortex core and $< 1\%$ outside the vortex core, for a 95% confidence level, for all velocity components under any given test case.

IV. TANGENTIAL VELOCITY DISTRIBUTION

Figure 7 presents the tangential (or swirl) velocity field at $x/\overline{c} = 2.5$ for $\alpha = 4°$, $8°$, and $10°$. The vortex is observed to transition farther inboard with both downstream distance and angle of attack.

Figure 8 shows the averaged tangential velocity distributions for $\alpha = 4°$ and $8°$ and $x/\overline{c}$, where the suction and pressure side of the vortex relative to the wing have been indicated. Distributions have been averaged over 36 radii equispaced around the vortex centre ($r/\overline{c} = 0$; which coincides with both $u_\theta/U_\infty = 0$ and peak H_x). The vortex core radius is defined, at any azimuth, as the distance between the vortex centre and the peak tangential velocity. Inside the vortex core, the swirling flow's behaviour is approximately linear, while outside the vortex core the swirl velocity varies inversely with the radial distance asymptotically approaching zero.

Within the vortex core, a secondary structure is consistently observed at $\approx 0.22r_c$ of the core radius (here, $r/\overline{c} \approx \pm 0.0035$), indicated by a point of inflection in an otherwise linear profile. This inflection (indicated by arrows) is particularly clear for $x/\overline{c} = 2.5$ for all α. Such double-core, or layered-core, structures have been previously observed by Devenport et al.[35], who argues that the double-core structure is a remnant of the vortex's initial conditions imposed by a blunt or squared wingtip - indeed, the wingtip of the wing model used in this work is squared, and not rounded. Engel[68] demonstrated the formation of the main wingtip vortex on the suction side of the wing, accompanied by the development of strong secondary vortices from the pressure side of the squared wingtip. Devenport et al.[35] suggested that vorticity associated with pressure side vortices become entrained, wrapping up into an annulus around, and merging with, the primary vortex core. This diffusive merging of primary and secondary wingtip vortices, leading to a multi-structured core, has also been discussed by Philips[16]. While multi-structured cores are theorised and discussed, there are sparse experimental observations, with little information regarding the actual structure, development, or behaviour present in the literature.

Independent of angle of attack, the early vortex peak tangential velocity on the suction-side, relative to the pressure side, of the wing is up to 16% higher at $x/\overline{c} = 1.35$; implying a continuously evolving vortex. This difference decreases with downstream distance as the vortex rolls-up further, circumferentially distributing the velocity field around the core and becoming increasingly more isolated from the vortex sheet. Figure 8 illustrates that for the angles of attack presented, the peak tangential velocities on the pressure-side approach an equivalent magnitude to those observed on the suction-side as $x/\overline{c} = 2.5$ is approached, and an axisymmetric tangential velocity distribution is neared - unhindered by the vortex sheet.

Variation in the vortex peak tangential velocity with downstream distance as a function of wing angle of attack is presented in Figure 9(a). Over $0° \leq \alpha \leq 6°$ (the linear lift region) a linear relationship is observed between the peak tangential velocity and angle of attack. As the wingtip begins to develop light separation at approximately $\alpha = 8°$ to $9°$, the tangential velocity for any given $x/\overline{c}$ station is seen to plateau. Further increases in the angle of attack ($\alpha > 9°$), deepening wingtip stall, leads to the transport of separated flow into the wingtip vortex - forming a large and slower decaying vortex system. Figure 9(b) rearranges the peak tangential velocity illustrating the decay as a function of downstream distance. The highest swirl velocities, and highest rates of decay with downstream distance are observed

for $\alpha = 8°$.

V. VORTEX CORE SHAPE

As previously stated, the vortex core radius, r, is defined as the distance between the vortex centre ($r/\overline{c} = 0$) and the point of maximum peak tangential velocity. In this work, the vortex core shape is presented as a locus of points defining the circumferential maximum tangential velocity contour around the vortex centre. Thus, the vortex core edge has been defined from 36 radii equispaced around the vortex centre. From this, different values of the core radius are identified depending on the orientation (with θ_v as the azimuthal coordinate) of the cut along which the swirl velocity is measured. Ramasamy et al.[62] found that just two data slices across the tip vortex (thereby producing four profiles) provided an acceptable measurement of the vortex's mean core radius, r_c. Errors in assessing the vortex core dimensions/shape are inherently dominated by observational systematic error of the vector field grid ($r_c \pm 0.7mm$); more information regarding this is provided in Appendix XI A.

In Figure 10, the radius values at each $x/\overline{c}$ plane are plotted as a function of θ_v for $\alpha = 4°$ and $8°$. In the present reference frame system the vortex rotates anti-clockwise. As qualitatively assessed in Figure 7, each angle of attack indicates the vortex core shape is axisymmetric, growing in size with both angle of attack and downstream convection - this is true for all α. It could be argued that there is a slight elongation of the vortex along $\theta_v = 45°$ and $225°$; this could be attributed to interactions and/or diffusive merging with the wing vortex sheet.

Variation in the mean vortex core radius as a function of angle of attack and downstream distance is presented in Figures 11(a) and 11(b), respectively. In Figure 11(a), a linear rate of growth is observed in the mean vortex core radius with angle of attack for any given downstream plane over the range $0° \leq \alpha \leq 8°$ (which coincides with the linear lift region of the wing). With the development of separation at the wingtip, the core radius reduced in size for both $\alpha = 9°$ and $10°$, relative to $\alpha = 8°$. In addition, the rate for the vortex growth is also reduced. It is interesting to note that the rate of vortex core growth is lower for $\alpha = 10°$ than for $\alpha = 8°$; this is clearest when comparing the farthest downstream station, $x/\overline{c} = 5.418$. It is also noticed that at the upstream locations (*e.g.* $x/\overline{c} = 1.35$), the vortex for $\alpha = 8°$ is smaller than that for $\alpha = 10°$. The only explanation that can

currently be attributed to this is that between $\alpha = 8°$ and 10° the progression of stall at the wingtip over the outboard wing alters the load distribution such that at $\alpha = 10°$ the early vortex development changes. For angles of attack $> 10°$, rapid vortex growth is observed as the wingtip stall deepens further and a less well defined, and subsequently weaker, vortex forms with a increased radius; refer to Skinner and Zare-Behtash[55] for further information regarding lift and stall behaviour.

Figure 11(b) presents the rate of the mean vortex core radius with downstream distance. It is observed that for all angles of attack there is a linear rate of growth with downstream propagation of the vortex; it is highlighted that while $\alpha = 12°$ and 14° are not shown here, they also display a linear growth with downstream propagation which is curious considering the deepening wingtip separation. Examining Figure 11(b), it is noticed that the rate of vortex growth with downstream distance increases with angle of attack over the linear lift range ($0° \leq \alpha \leq 8°$). This is due to higher angles of attack increasing the tangential velocities (hence increasing the vortices circulation and Reynolds number) and increasing the turbulent diffusion around the vortex core. The reduced rate of growth is again noticed for $\alpha = 10°$. These observed linear growth rates appear to be more indicative of laminar diffusion rates. An explanation for these vortex laminar growth rates is provided and discussed in Section VIII.

VI. AXIAL VELOCITY DISTRIBUTION

In the physical flow field of an axisymmetric trailing vortex from a conventional planar wing, the fluid surrounding the vortex core is layered with the boundary layer fluid entrained from the wake sheet from the wing surface. This introduces strong shear-layers and viscous losses that contribute to the deceleration of the flow. Spalart[20] indicates that there must be a balance between viscous effects and inviscid acceleration of the axial flow; *i.e.* large values of local circulation will result in an excess velocity, while low values will result in a velocity deficit, of the axial flow field.

For planar wings, Bailey et al.[69] demonstrated that in the very early stages of the vortex formation, the pressure in the vortex core gradually decreases along the vortex axis generating a favorable pressure gradient which accelerates the core fluid in the streamwise direction. This results in a jet-like core with an axial velocity excess[35]. Farther downstream, viscous

effects decelerate the flow, yielding a wake-like velocity deficit developing within the core. It has also been observed that axial velocity gradients introduce a possible mechanism for the production of turbulence within the core[36,70]. All the trailing vortices examined in this study exhibit a wake-like structure, and are considered too far downstream ($x/\overline{c} \geq 1.35$) to exhibit a jet-like vortex core.

Figure 12 presents the mean axial velocity contour for $x/\overline{c} = 2.5$ at $\alpha = 4°$, $8°$, and $10°$. As discussed, the vortex core axial velocity demonstrates a velocity deficit; however, outside of the vortex core (on the pressure/inboard side of the vortex) a velocity excess is noticed. This velocity excess is located in a pocket of flow between the vortex and the trailing wake sheet, and is observed to be stronger in closer proximity to the wing (where the vortex and wake sheet are closest), and for moderate angles of attack. Batchelor[15] predicted the existence of axial velocity excess trailing vortex systems, both inside and outside of the core, capable of exceeding the freestream velocity. In the three-dimensional vortex, the swirling mass of air is accelerated axially as it is compressed between the highly viscous regions of the wake sheet and the vortex core. With stronger vortices (higher tangential velocities) the region of excess velocity is seen to grow while the magnitude remains fairly constant at $u_x/U_\infty \approx 1.08$. As the vortex convects downstream and continues to roll-up, the vortex core becomes increasingly more isolated from the wake sheet, hence the velocity excess decreases, tending to U_∞.

Figure 13 shows the averaged axial velocity distribution through the vortex core for $\alpha = 4°$ and $8°$ at all $x/\overline{c}$ stations, where the suction and pressure sides of the wing have been indicated. As before, distributions have been averaged over 36 equispaced radii around the vortex centre. Inside of the core, the axial flow demonstrated a velocity deficit, with the velocity excess noticed between the range $0.01 \leq x/\overline{c} \leq 0.03$. Furthermore, as with the tangential velocity profile, a double gradient structure is observed near each vortex core centre at $\approx 0.22 r_c$ ($r/\overline{c} \approx \pm 0.0035$).

Variation of the peak axial deficit with downstream distance as a function of angle of attack is presented in Figure 14(a). Over the linear lift region, the axial deficit increases until stall onset is approached, at which point the peak velocity deficit in the core is shown to decrease. This result was also observed by Gerontakos and Lee[50]. Figure 14(b) illustrates that the peak core deficit shows a general decreasing trend (*i.e.* increasing core axial flow) as the vortex travels downstream, indicative of a favorable pressure gradient ($\partial\rho/\partial x < 0$) along

the vortex axis. Furthermore, the decay of the velocity deficit at the centre of the vortex core evolves approximately with $x^{-1}log(x)$, which coincides with the asymptotic variation proposed by Batchelor[15] for a fully developed trailing vortex. Similar observations have been made by Philips and Graham[71], and Sousa and Pereira[60], who indicate that the development of the axial pressure gradient along the vortex is driven by the axial variation of the swirl velocity, which in turn gives rise to the core axial velocity gradient. These mechanisms provide a balance between inertial and pressure gradient forces.

In consideration of this balance, such a pressure distribution is likely responsible for the appearance of the aforementioned axial velocity excess outside of the vortex core - highlighted in Figure 12. Similar regions of velocity excess have been identified in other experimental campaigns[37,60,72].

VII. VORTICITY DISTRIBUTION

Streamwise vorticity, ω_x, of the trailing vortex at $x/\bar{c} = 2.5$ for $\alpha = 8°$ is shown in Figure 15. Here, the spiral structure of the wingtip vortex merging with the wake sheet is visible. For planar wings, the innermost portion of the spiral (the core) becomes axisymmetric and the effects of diffusion form a merged region with a smooth distribution of vorticity; the vortex core, core edge, outer vortex, and vortex wake sheet have been labeled. Note that in the current frame of reference, the vortex rotates anti-clockwise.

The vorticity distributions for $\alpha = 4°$ and $8°$ at all streamwise stations are presented in Figure 16. For each angle of attack, the peak vorticity at the centre of the vortex core is observed to persist as the vortex convects downstream with only very slight rates of decay observed over the $1/35 \leq x/\bar{c} \leq 5.418$ range. However, with downstream propagation of the wingtip vortex, the core develops into two distinct structures meeting at $\approx 38\%$ of the core radius, with the outer portion of the vortex dissipating at a faster rate. The inner vortex core structure ($\leq 0.38r_c$) appears insulated by the outer vortex core structure, acting as a buffer region which disperses with downstream distance via viscous/turbulence diffusion mechanisms. This explanation helps to clarify why the peak vorticity does not reveal any significant rate of decay with angle of attack or downstream propagation, as illustrated in Figures 17(a) and 17(b), respectively. The persistence and stability of peak streamwise vorticity with downstream position in the near field vortex development has also

been observed by Ramaprian and Zheng[37] and Yang and Shengjin[73] for planar wings.

From Figure 17(a), the peak vorticity over the range $0° \leq \alpha \leq 6°$ exhibits a linear increase for each angle of attack at any given downstream plane. Progressing into stall onset ($\alpha > 8°$), the peak vorticity is recorded to plateau and then steeply drop off as the wing stall deepens and the weaker wingtip vortex is formed. This behaviour is reflected in Figure 17(b) which also highlights the slow decay of the vorticity with downstream distance. It is also noticed that vorticity decay is lowest for stronger trailing vorticies, which experience the highest tangential velocities.

VIII. TURBULENT PROPERTIES IN THE VORTEX CORE

A. Turbulent Kinetic Energy Evolution

In this section, turbulent properties of the vortex core are discussed; however, it is emphasized that due to the $200Hz$ data rate of the sPIV system, only low frequency fluctuations $< 100Hz$ are examinable.

The turbulent kinetic energy (TKE) development for $\alpha = 0°$, $4°$, $8°$, and $10°$ are presented in Figure 18, for planes $x/\bar{c} = 1.35$ and 5.814, providing a concise description of how the TKE varies with both angle of attack and downstream distance; note that these are not circumferentially averaged, presenting a single data slice along $z/\bar{c}$ at $y/\bar{c} = 0$. The depression at the core centre indicates that relaminarisation of the inner vortex core has occurred. Chow et al.[36] observed a similar reduction of the turbulence within the trailing vortex core in the near field, attributing this to the development of a laminar rotation within the vortex core as a result of progressive damping of turbulent fluctuations. Trailing vortices, in particular the vortex cores, are capable of relaminarisation due to the flow induced by rotation with which the contribution of the turbulent fluctuation to the mean flow dynamics become negligible[74]. Under such circumstances the inner core flow approaches a laminar state; it will carry residual turbulence inherited from upstream flow conditions, but this has been rendered passive. The driving mechanism for relaminarisation are the centrifugal motions of turbulent patches away from the inner core, subsequently giving rise to high flow curvature and the suppression of turbulence energy.

Work by Martin[75,76] has shown evidence that the trailing vortex structure is neither

fully laminar, nor fully turbulent, but is instead in a continuous state of dynamic evolution with an inner core exhibiting slow laminar diffusion surrounded by a region of relatively accelerated turbulent diffusion. This is observed in Figure 18 where the dip at the centre of the vortex ($r/\overline{c} = 0$) signifies a laminar inner core structure, while the peaks at either side (at $\approx 0.24r_c$) indicate an annulus of relatively higher turbulent flow enveloping it. Thus, the vortex propagates downstream with the dominant diffusion mechanism driven by viscosity rather than turbulence[77].

This explains the persistence and strength of vortices moving downstream. Rotations within the vortex core can strongly inhibit turbulence transport of the fluid leading to a stratified flow field[78]. Trailing vortices, and in particular vortex cores, are examples of stratified relaminarised flows induced by the fluid rotation in which the contribution of the turbulent fluctuations to the mean flow dynamics becomes suppressed, and a laminar flow is established[74].

Figure 18(a) shows the increase of TKE with angle of attack at $x/\overline{c} = 1.35$, the closest sPIV plane to the wing trailing edge. At $\alpha = 10°$, the relatively shallower dip in the TKE at the centre is attributed to the increased interaction of the primary core with secondary vortices which are stronger and more persistent at higher angle of attack[79], and separated flow from the wingtip. These induce high disturbances into the primary vortex core and increase the TKE. At the downstream plane, $x/\overline{c} = 5.418$, shown in Figure 18(b), the peak turbulence levels are seen to persist for each angle of attack. The radial diffusion of the turbulent annulus grows while the laminar inner core shows little radial growth.

The turbulent dissipation of trailing vortices can be broadly explained as a fluidic system tending towards a state of lower kinetic energy equilibrium by dissipating TKE while conserving angular momentum[78]. Bradshaw[80] quantified this analogy between rotation and stratification. Using energy arguments, an expression for the local strength of the analogous stratification in a rotating flow was developed, represented as an equivalent gradient Richardson number. This analogy, formulated in terms of a Richardson number, can be applied to further the understanding of viscous turbulent vortices. The Richardson number, Ri, is the ratio of the potential to kinetic energy in the stratified flow. The local gradient Ri is defined as[78]:

$$Ri = 2S_p(S_p + 1) \tag{4}$$

where the Bradshaw non-dimensional shape parameter S_p is given in terms of the tangential

velocity and its gradient[80]:

$$S_p = \left(\frac{u_\theta}{r}\right) / \left(\frac{du_\theta}{dr}\right) \tag{5}$$

The measured distribution of Ri through the respective vortex as a function of r/r_c for $\alpha = 0°$, $4°$, $6°$, $8°$, and $10°$ at downstream station $x/\bar{c} = 2.5$ is shown in Figure 19(a). The result infers that the high streamline curvature around the vortex core prevents the formation of large scale turbulent eddies at the core edge ($r/r_c = 1$); this result is observed for all angles of attack, including those over the linear lift range of the wing ($0° \leq \alpha \leq 6°$), stall onset ($\alpha \approx 8°$), and post-stall ($\alpha = 10°$).

The existence of large eddies would contribute to the turbulent diffusion of vorticity away from an otherwise laminar core. As the Richardson number exceeds a critical value, based on the vortex Reynolds number ($Re_\nu^{1/4}$), where the vortex Reynolds number is defined as:

$$Re_\nu = \Gamma \nu^{-1}, \tag{6}$$

it is inferred that the streamline curvature around the vortex core is sufficiently high enough to prevent the formation and/or transport of large scale turbulent eddies (see Figure 19).

In other words, where $Ri > Re_\nu^{1/4}$, the flow is so strongly stratified and smooth, that turbulence is heavily damped[78]. At $r/r_c = 1$, large-scale high energy eddies have insufficient kinetic energy to entrain fluid across the boundary, while at $r/r_c < 1$ Kolmogorov micro-scale eddies are unable to engulf fluid and increase mixing[81]. Hence, for $r/r_c < 1$ diffusion is the only possible transport mechanism. According to this theoretical model, the diffusive flux is determined by a surface renewal frequency of either large-scale or small-scale eddies[82]. These two eddy sizes in turn correspond to the two possible limits of vortex persistence. If the large-scale eddies are not persistent with respect to the surface, the flux is determined by the smallest eddies. At this condition, the radial momentum transport would be proportional to $Re_\nu^{1/4}$.

Consequently, the result of Figure 19(a) supports the suggestion that core relaminarisation has occurred, such that over the range $1.35 \leq x/\bar{c} \leq 5.418$, the vortex core is expected to be subjected to only viscous diffusion for the angle of attack range considered. This explains why the vortex core grows/dissipates at a slow, viscous, laminar rate, as previously examined with consideration towards the tangential velocity and vorticity decay, and radial growth, unaffected or perturbed by the surrounding turbulent flow exhibiting persistent behaviour. Similar profiles to that shown in Figure 19(a), for the local Richardson number,

are obtained at all α, for all $x/\bar{c}$ planes, at any azimuthal orientation of data cut through the respective vortex core. Furthermore, the value of Ri at $r/r_c = 1$ is noticed to generally increase as the vortex propagates downstream, indicating stronger stratification at the core edge. This is illustrated for $\alpha = 8°$ in Figure 19(b). This suggests that the laminar core, over the $x/\bar{c}$ range investigated, becomes increasingly less vulnerable to turbulent dissipation as the trailing vortex continues to develop over the near-field wake.

B. Reynolds Shear Stress and Strain Rates

Evolution of the in-plane Reynolds shear stress, $\overline{v'w'}$, for the trailing vortex at $\alpha = 8°$ for downstream stations $x/\bar{c} = 1.35$, 2.5, and 5.418 are presented in Figure 20; the respective mean core vortex radii have been superimposed for reference. The shear stress intensity is observed to increase for planes closer to the wing trailing edge and for increasing angle of attack. For planes $x/\bar{c} \leq 2.5$ the axisymmetry of the vortex is visible, while further downstream at $x/\bar{c} = 5.418$ shear stresses exhibit strong decay and asymmetry. Examination of the shear stress indicate a bi-modal four-lobed pattern with peak values at two different vortex core radii, which are clearest for $x/\bar{c} = 2.5$: an inner maximum at $\approx 0.24r_c$, and an outer maximum occurring at $\approx 0.94r_c$. Considering that shear stress is primarily caused by friction between fluid particles due to viscosity, it is interesting that peak stresses occur near the vortex core sub-structure (at $r \approx 0.22r_c$), and the vortex core boundary itself (at $r = r_c$).

Figure 21 illustrates the evolution of the in-plane Reynolds shear stress with downstream distance for $\alpha = 4°$ and 8°, taking data slices at 135° from the sPIV data presented in Figure 20 (through the positive lobes). The shear stress intensity is observed to decay moving away from the wing for the angles of attack shown. The shear stress reaches its maximum at $\approx 0.94r_c$, rapidly reducing to zero within 1.5 core radii for the respective vortex axis.

The eddy viscosity distribution (i.e. the production of turbulence) is dependent upon the Reynolds shear stress, not explicitly upon the turbulence intensities[63]. As a result, even though the in-plane turbulent fluctuations both reach a maximum at the centre of the vortex, their product ($\overline{v'w'}$) is found to reach a minimum, and is a consistent finding among other studies[36,63].

The shear stresses drive the shear strain rates, and subsequently contribute to the viscous

dissipation of the kinetic energy. The shear strain rate is the deformation of the fluid caused by elongation, compression, volume change, or angular distortion due to an external force (shear stress), and thus expresses how the relative velocity of the medium changes (*i.e.* velocity gradient). The contours of the shear strain rates, corresponding to the Reynolds shear stresses presented in Figure 20, are reported in Figure 22.

The Reynolds shear stresses (Figure 20), and their associated shear strains (Figure 22), each exhibit a bi-modal four-lobed pattern with alternative positive/negative signs - this has significant physical meaning, especially when orientated off-axis from one another. In the case of the $\overline{v'w'}$ components, the lobes are at approximately 45° to the $y/\overline{c}$ and $z/\overline{c}$ axes, whereas the component lobes of ε_{yz} are aligned with these axes. The difference in orientation between the stress and strain indicates that a linear eddy viscosity assumption would be invalid. An interesting point, in light of this, is that linear eddy viscosity models used in Reynolds Averaged Navier-Stokes (RANS) solutions assume an isotropic distribution of eddy viscosity by representing the entire stress tensor as a scalar (*e.g.* with $k-\varepsilon$ and $k-\omega$ models). Such simulation modeling would be misleading in regard to the turbulence distributions within the vortex core as these models, which assume a linear eddy viscosity, would align the axis of the Reynolds shear stresses and associated shear strain rates. Churchfield and Blaisdell[83] demonstrated this limitation in RANS solutions. Subsequently, they modified the Spalart-Allmaras model to account for streamline curvature, successfully modeling the lag between the mean strain rate and respective Reynolds stresses[84].

Visible from Figure 22, it is observed that the shear strain rates form a double-lobed pattern with two local maxima - similar to that found with the shear stresses. Additionally, higher angles of attack, and greater downstream distance, exhibit vortices with a broader distribution of high shear strain rates. Symmetry of the trailing vortex is maintained under all conditions. The inner maximum occurs at $\approx 0.3r_c$, and the outer occurs at $\approx 1.22r_c$, with consistency for all angles of attack and downstream stations; a local minima exists at $\approx 0.47r_c$. This is illustrated in Figure 23, where each data slice has been taken horizontally through the positive lobes of the shear strains presented in Figure 22. From Figure 23, the outer region of shear strain dissipates and weakens with downstream distance as the vortex core grows. The inner-lobe shear strain rates are seen to persist with downstream distance as they are related to the relaminarised portion of the inner vortex core.

IX. SUMMARY OF CORE STRUCTURE

The structure of the vortex core observed in this work is consistent for all angles of attack and downstream location; this structure is summarised in Figure 24. Similar structures are noted to have been observed, but with lower spatial resolution[35,38]. The overbearing description of the vortex agrees with the work of Philips[16], who studied the turbulent roll up of the vortex sheet. Philips[16] divided the vortex region into three concentric regions; however, stated that multi-structured/stratified cores could be expected to reach a state of equilibrium. The three dominant regions of the vortex are summarised as:

1. The innermost core, dominated by viscous effects which decrease the tangential velocity linearly to zero at the core centre. The rotation here is close to solid-body rotation and the Reynolds stresses will tend to zero with the square of the distance from the centre.

2. The second region is located around the point of peak tangential velocity (at the vortex core radius, r_c). Here, the viscous effects are small and in this highly strained turbulent region a logarithmic law for circulation applies[14].

3. In the outer region, the flow is turbulent, the tangential velocity decays as a potential vortex (as $1/r_c$)) and the Reynolds stresses approach zero as $1/r_c^2$.

X. SELF-SIMILAR VORTEX BEHAVIOUR

Investigations[37,38] of axisymmetric turbulent vortex structures, such as those observed in this work, have demonstrated that the circulation distribution of the first two regions follow universal, self-similar, behaviors in the near field, described by semi-empirical laws. The radial distribution of the circulation, Γ, of the trailing vortex, normalised by the circulation of the vortex core, Γ_c, as a function of $log(r/r_c)$ for $\alpha = 8°$ over $1.35 \leq x/\overline{c} \leq 5.418$, is presented in Figure 25(a). Additionally, 25(b) shows the variation of the scaled circulation profiles for various α at $x/\overline{c} = 2.5$. Distributions of circulation have been calculated by integrating the tangential velocity, where circulation is the macroscopic measure of fluid swirl, and is a precise measure of the average flow of fluid along a given closed curve.

From the distributions illustrated in Figures 25(a) and 25(b), the scaled circulation within the vortex core follows a $\Gamma \propto r^2$ profile for $r/r_c < 0.4$, and varies logarithmically for $0.5 \leq r/r_c \leq 1.4$. For $r/r_c > 1.4$, Γ continues to vary with both $x/\overline{c}$ and α, suggesting that the vortex is still gaining a slow addition of vorticity to the outermost layers of the vortex from the shear-layer arriving from the inboard regions. The self-similar universal circulation behaviour observed in the core region is of particular interest, as it indicates that the vortex is well developed[38].

Hoffman and Joubert[14] demonstrated that a developed turbulent vortex should be expected to exhibit a universal inner-scaled circulation profile. Their work presents empirical curve-fit relationships that describe the inner core region, as the region where the Γ/Γ_c distribution is logarithmic, as:

$$\Gamma/\Gamma_c = A(r/r_c)^2 \quad for \quad r/r_c < 0.4 \tag{7}$$

and

$$\Gamma/\Gamma_c = B\ log(r/r_c) + C \quad for \quad 0.5 \leq r/r_c \leq 1.4 \tag{8}$$

where A, B, and C are empirical curve fit constants.

Furthermore, for $1.35 \leq x/\overline{c} \leq 5.418$, all Γ/Γ_c profiles within the range of $0 \leq r/r_c \leq 1.2$ collapse together, and can be approximated by a sixth-order polynomial (similar to that reported by Ramaprian and Zheng[37]) with a self-correlation coefficient of 0.998:

$$\Gamma/\Gamma_c = 1.756(r/r_c)^2 - 1.044(r/r_c)^4 + 0.263(r/r_c)^6 \tag{9}$$

Figures 25(c) compares the self-similar core flow structure of the vortex at $\alpha = 8°$ at $x/\overline{c} = 2.5$ with the empirical relationship described (curve fit constants used: $A = 1.666$ in Equation 7; $B = 2.010$ and $C = 0.972$ in Equation 8). Results are consistent with those found elsewhere[14,16,37,38,46,50]. A direct comparison of the levels of radial growth of the vortex strength, $\Gamma/U_\infty\overline{c}$, of the trailing vortex for different angles of attack at $x/\overline{c} = 2.5$ is summarized in Figures 25(d). This shows the increased level of circulation within the core with angle of attach from $\alpha = 0°$ to $8°$, after which for $\alpha = 10°$ the circulation is noticed to reduced slightly due to weakened vortex formation driven by wingtip stall progression.

XI. CONCLUSIONS

An experimental investigation has been conducted to assess the development and structure of the near-field trailing vortex shed from a swept-tapered planar wing; analogous of a typical mid-sized commercial aircraft wing topology, representing a 10% scale model. Stereoscopic particle imaging velocimetry (sPIV) has been utilised to conduct the investigation through comparing the trailing vortex core development at several angles of attack at various downstream stations at a fixed Reynolds number ($Re = 1.5 \times 10^6$). Vortex meander has been corrected for using helicity based spatial localisation of the instantaneous vector fields, enabling the accurate assessment of vortex translation, tangential velocity, axial velocity, vorticity, and turbulent qualities.

Examination of the planar wing trailing vortex system over the downstream range $1.35 \leq x/\overline{c} \leq 5.418$ identified a persistent axisymmetric vortex core for which the peak tangential velocity, mean core radius, and peak vorticity increased linearly with angle of attack over the linear lift range of the wing. Decay rates of the vortex are also observed to be linear, dissipating with rates indicative of laminar diffusion mechanisms. The turbulent kinetic energy evolution of the vortex core indicated that relaminarisation of the inner core had occurred for all α through all downstream stations. Additionally, independent consideration of the streamline curvature around the core via the Richardson number indicated a stratified laminar core structure, within which large scale turbulent eddies are unable contribute to the turbulent diffusion of vorticity away from the core. This behaviour is typical of conventional planar wing trailing vortices[85], and explains the persistence of the vortex core observed due to its laminar growth rates where viscous diffusion is the only possible transport mechanism.

The vortex was also seen to exhibit a distinct double-layered core structure, the likes of which were first considered by Devenport[35]. Observation of such behaviour was possible due to the sufficient resolution provided by the sPIV. Based on observations and analysis from the literature, the formation of such a core structure is hypothesized to be driven by the wing's squared-off wingtip. The normalised circulation distribution within the vortex core exhibits self-similar behaviour, implying that the behaviours and structure observed is independent of Reynolds number.

Data Availability Statement

Data that support the findings of this study are openly available in '*Half aircraft model wind tunnel data, Shaun Skinner*' at [http://dx.doi.org/10.5525/gla.researchdata.1036]. Additional data sets are available from the corresponding author upon request.

Acknowledgments

The authors would like to express our gratitude and appreciation to the National Wind Tunnel Facility (EPSRC Grant number: EP/L024888/1) at the University of Glasgow. We would also like to thank all of the technical staff at the University of Glasgow, especially Mr. Neil Owen. Gratitude also goes to Zephyr Business Services (Grant number: 74603) and the Royal Aeronautical Society Centennial Scholarship (Grant number: 21-657/A-SKI) for funding this work.

Appendix

A. sPIV Convergence and Uncertainty

The assessment of the statistical convergence for selected vortex flow properties is performed, adopting the helicity centering method with up to 1800 velocity vector fields of the planar wing reference case. The effects of varying the number of instantaneous velocity vector fields enables the determination of the minimum number of samples that are required to achieve statistical convergence. Peak uncertainties exist in clusters within the vortex core[57]; the evaluation of the uncertainties presented in here are to be taken as an overestimation of the global measurement as they only represent peak values.

The in-plane and out-of-plane velocity vector fields show a distinct and converged shape with only 25 samples, however, many more samples ($\approx$ 250) are required to bring the uncertainty error within the core down to $\approx$ 10% and reach a smooth, fully converged vector field. This is observed in Figures 26(a) and 26(b), where the combined uncertainty is inversely proportional to the number of samples, N. Averaging over the full 1800 samples brings any maximum velocity vector uncertainty within the planar core vortex below 4% for any given test case. Outside of the vortex core, uncertainties are below 1%. Maximum uncertainly for any resulting vorticity field is $< 3\%$.

A cubic interpolation of 36 equispaced radii around the vortex centre is performed to evaluate the circumferential mean of the vortex core radius; the value and associated uncertainty, as a function of N, is given in Figures 26(c). There is no distinct trend observed for the variation in the vortex radius with sample range N. This is due to the observational systematic error of the vector field grid dominating errors associated with measuring the vortex core radius ($r_c \pm 0.7mm$). The variation in the mean core radius observed with number of samples N ($0.0168r_c/\overline{c}$ to $0.0192r_c/\overline{c}$) equates to a change in the mean radius of $\approx 0.66mm$. The uncertainty of the vortex measurement does not exceed 6% for any range of N (*i.e.* indicating robust identification of peak tangential velocities), where for $N \geq 1000$ the maximum uncertainty is approximately 4% - this holds true for all test cases.

Figure 26(d) illustrates that at least 750 samples are required to converge second-order turbulence characteristics, while at least 1200 samples are required to bring the peak shear strain rate uncertainty below 8%. Under the same conditions, the Reynolds shear stress

converge to a peak uncertainty of 5.5%.

References

[1] V.V. Vyshinsky. Aircraft Vortex Wake and Airport Capacity: Collection of Papers. *Air and Space Europe*, 3:206–208, 2001.

[2] K. Hunecke. Wake Vortex Control - A Challenge for Large Transport Aircraft. *Air and Space Europe: Air Transport Safety*, 3:209–213, 2001.

[3] J.N. Hallock and F. Holzäpfel. A Review of Recent Wake Vortex Research For Increasing Airport Capacity. *Progress in Aerospace Sciences*, 98:27–36, 2018.

[4] Aircraft Accident Report: NTSB-AAR-81-1. *United States National Transport Safety Board*, 1981.

[5] Wake Turbulence Encounter - Collision with Terrain. *Transport Safety Board of Canada Aviation Investigation Report: A09P0187*, 2009.

[6] T. Gerz, F. Holzäpfel, and D. Darracq. Commercial Aircraft Wake Vortices. *Progress in Aerospace Sciences*, 38:181–208, 2002.

[7] T. Gerz, F. Holzäpfel, W. Bryant, F. Köpp, M. Frech, A. Tafferner, and G. Winckelmans. Research towards a wake-vortex advisory system for optimal aircraft spacing. *Comptes Rendus Physique*, 6(4-5):501–523, 2005.

[8] Flightpath 2050 Europe's Vision for Aviation. In *European Commission Report of the High Level Group on Aviation Research*, 2011.

[9] Airbus. *Airbus Global Market Forcast: Cities, Airports, & Aircraft 2019-2037*. Blagnac Cedex, France, 2019.

[10] J. Hemmerdinger. Out With the Old Jets? How Virus Led Fleet Descisions Will Impact OEMs, Aftermarket Providers. *Flight Global*, 2020.

[11] M. Morrison. Transatlantic Traffic Keeps Biggin Hill's Head Above Water. *Flight Global*, 2020.

[12] United States Aviation Greenhouse Gas Emissions Reduction Plan, 2015.

[13] A. Allen and C. Breitsamter. Transport Aircraft Wake Influenced by a Large Winglet and Winglet Flaps. *Journal of Aircraft*, 45(2):686–699, 2008.

[14] E.R. Hoffmann and P.N. Joubert. Turbulent Line Vortices. *Journal of Fluid Mechanics*, 16(3): 395–411, 1963.

[15] G.K. Batchelor. Axial Flow in Trailing Line Vortices. *Journal of Fluid Mechanics*, 26(4): 645–658, 1964.

[16] W.R.C. Phillips. The Turbulent Trailing Vortex During Roll-Up. *Journal of Fluid Mechanics*, 105:451–467, 1981.

[17] S.I. Green and A.J. Acosta. Unsteady Flow in Trailing Vortices. *Journal of Fluid Mechanics*, 227:107–134, 1991.

[18] G.W. Brune. Quantitative low-speed wake surveys. *Journal of Aircraft*, 31(2):249–255, 1994.

[19] K. Kusunose. Development of a universal wake survey data analysis code. *15th Applied Aerodynamics Conference*, pages 617–626, 1997.

[20] P.R. Spalart. Airplane Trailing Vortices. *Annual Review of Fluid Mechanics*, 30:107–138, 1998.

[21] L. Jiang, J. Cai, and C. Liu. Large Eddy Simulation of Wing Tip Vortex in the Near Field. Technical report, University of Texas, Arlington., 2007.

[22] P. Anusonti-Inthra and M. Floros. Coupled CFD and Particle Vortex Transport Method: Wing Performance and Wake Validations. In *38th Fluid Dynamics Conference and Exhibit; AIAA 2008-4177*, Seattle, Washington, 2008.

[23] D.M. Birch. Self-Similarity of Trailing Vortices. *Physics of Fluids*, 24(2), 2012.

[24] M.J. Churchfield and G.A. Blaisdell. Reynolds Stress Relaxation Turbulence Modeling Applied to a Wingtip Vortex Flow. *AIAA Journal*, 51(11):2643–2655, 2013.

[25] J.E. Lombard, D. Moxey, S.J. Sherwin, J.F.A. Hoessler, S. Dhandapani, and M.J. Taylor. Implicit Large-Eddy Simulation of a Wingtip Vortex. *AIAA Journal*, 54(2):506–518, 2016.

[26] R. Paoli and H. Moet. Temporal Large-Eddy Simulations of the Near-Field of an Aircraft Wake. *Open Journal of FLuid Dynamics*, pages 161–180, 2018.

[27] P. Ranjan and P.J. Ansell. Computational Analysis of Vortex Wakes Without Near-Field Rollup Characteristics. *Journal of Aircraft*, 55(5):2008–2021, 2018.

[28] A.C. Devoria and K. Mohseni. Vortex Sheet Roll-Up Revisited. *Journal of Fluid Mechanics*, 855:299–321, 2018.

[29] P. Ranjan, P.J. Ansell, and K.A. James. Optimal Hyperelliptic Cambered Span Configurations for Minimum Drag. *Journal of Aircraft*, 56(1):356–368, 2019.

[30] A. Asnaghi, U. Svennberg, and R.E. Bensow. Large Eddy Simulations of Cavitating Tip Vortex Flows. *Ocean Engineering*, 195(106703), 2020.

[31] A. Asnaghi, U. Svennberg, R. Gustafsson, and R. Bensow. Investigations of Tip Vortex Miti-

gation by Using Roughness. *Physics of Fluids*, 32(065111), 2020.

[32] T.B. Francis and J. Katz. Observations on the development of a tip vortex on a rctngular hydrofoil. *Journal of Fluids Engineering*, 110(2):208–215, 1988.

[33] K.W. McAlister and R.K. Takahashi. NACA 0015 Wing Pressure and Trailing Vortex Measurements. *Nasa Technical Paper 3151*, 1991.

[34] Y. Zheng and B.R. Ramaprian. An Experimental Study of Wing Tip Vortex in the Near Wake of a Rectangular Wing. *The U.S. Army Research Office, Report No. MME-TF-93-1*, 18, 1993.

[35] W.J. Devenport, M.C. Rife, S.I. Liapis, and G.J. Follin. The Structure and Development of a Wing-Tip Vortex. *Journal of Fluid Mechanics*, 312:67–106, 1996.

[36] J.S. Chow, G.G. Zilliac, and P. Bradshaw. Mean and Turbulence Measurements in the Near Field of a Wingtip Vortex. *AIAA Journal*, 35(10):1561–1567, 1997.

[37] B.R. Ramaprian and Y. Zheng. Measurements in Rollup Region of the Tip Vortex from a Rectangular Wing. *AIAA Journal*, 35(12):1837–1843, 1997.

[38] D. Birch, T. Lee, F. Mokhtarian, and F. Kafyeke. Structure and Induced Drag of a Tip Vortex. *Journal of Aircraft*, 41(5):1138–1145, 2004.

[39] H.J. Zhang, Y. Zhou, and J.H. Whitelaw. Near-Field Wing-Tip Vortices and Exponential Vortex Solution. *Journal of Aircraft*, 43(2):445–449, 2006. ISSN 0021-8669.

[40] M. Giuni and R.B. Green. Vortex Formation on Squared and Rounded Tip. *Aerospace Science and Technology*, 29(1):191–199, 2013.

[41] M.O. Memon, K. Wabick, and A. Altman. Wing Tip Vortices from an Exergy-Based Perspective. *Journal of Aircraft*, 52(4):1267–1276, 2015.

[42] S. Gunasekaran and A. Altman. Is There a Relationship Between the Wingtip Vortex and the Shear Layer? *54th AIAA Aerospace Sciences Meeting, AIAA 2016-1068*, 2016.

[43] D.J. Moreau and C.J. Doolan. An Experimental Study of Airfoil Tip Vortex Formation Noise. In *Proceedings of Acoustics 2016*, Brisbane, Australia, 2016.

[44] G.V. Iungo. Wandering of a Wing-Tip Vortex : Rapid Scanning and Correction of Fixed-Point Measurements. *Journal of Aircraft*, 54(5), 2017.

[45] M.O. Memon. *Wingtip Vortices and Free Shear Layer Interaction In The Vicinity of Maximum Lift to Drag Ratio Lift Condition*. PhD thesis, University of Dayton, 2017.

[46] H.C. Ghimire and S.C.C. Bailey. An Experimental Investigation of Wing-Tip Vortex Decay in Turbulence. *Physics of Fluids*, 29(3), 2017.

[47] Z. El-Ramly, W.J. Rainbird, and D.G. Earl. Wind Tunnel Measurements of Rolling Moment in a Swept-Wing Vortex Wake. *Journal of Aircraft*, 13(12):962–967, 1976.

[48] K.L. Orloff and D.L. Ciffone. Vortex Measurements Behind a Swept Wing Transport Model. *Journal of Aircraft*, 11(6):362–364, 1974.

[49] E. Ozger, I. Schell, and D. Jacob. On the Structure and Attenuation of an Aircraft Wake. *Journal of Aircraft*, 38(5):878–887, 2001.

[50] P. Gerontakos and T. Lee. Near-Field Tip Vortex Behind a Swept Wing Model. *Experiments in Fluids*, 40:141–155, 2006.

[51] C. Breitsamter. Wake Vortex Characteristics of Transport Aircraft. *Progress in Aerospace Sciences*, 47:89–134, 2011.

[52] O.A. Elsayed, W. Asrar, A.A. Omar, and K. Kwon. Evolution of NACA23012 Wake Vortices Structure Using PIV. *Journal of Aerospace Engineering*, 2012.

[53] G.E. Wroblewski and P.J. Ansell. Prediction and Experimental Evaluation of Planar Wing Spanloads for Minimum Drag. *Journal of Aircraft*, 54(5):1664–1674, 2017.

[54] S. Zhang, A.J. Jaworski, S.C. McParlin, and J.T. Turner. Experimental investigation of the flow structures over a 40 ° swept wing. *The Aeronautical Journal*, 123(1259):39–55, 2019.

[55] S.N. Skinner and H. Zare-Behtash. Study of a C-wing Configuration for Passive Drag and Load Alleviation. *Journal of Fluids and Structures*, 78:175–196, 2018.

[56] S.N. Skinner and H. Zare-Behtash. Semi-Span Wind Tunnel Testing Without Conventional Peniche. *Experiments in Fluids*, 58(163), 2017.

[57] S.N. Skinner. *Study of a C-wing Configuration for Passive Drag and Load Alleviation*. PhD thesis, University of Glasgow, 2018.

[58] LaVision. *DaVis 8 software - Product Manual*. Germay, 2012.

[59] M. Raffel, C.E. Willert, S.T. Wereley, and J. Kompenhans. *Particle Image Velocimetry: A Practical Guide*. Springer, 2nd edition, 2007.

[60] J.M.M. Sousa and J.C.F. Pereira. Rollup Region of a Turbulent Trailing Vortex Issued from a Blade with Flow Separation. *Experimental Thermal and Fluid Science*, 20:150–161, 2000.

[61] M. Ramasamy, R. Paetzel, and M.J. Bhagwat. Aperiodicity Correction of Rotor Wip Vortex Measurements. In *In American Helicopter Society 67th Annual Forum*, Virginia Beach, VA, 2011.

[62] M. Ramasamy, B. Johnson, T. Huismann, and J.G. Leishman. Digital Particle Image Velocime-

try Measurements of Tip Vortex Characteristics Using an Improved Aperiodicity Correction. *Journal of the American Helicopter Society*, 54(1), 2009.

[63] M. Ramasamy, B. Johnson, T. Huismann, and J.G. Leishman. Procedures for Measuring the Turbulence Characteristics of Rotor Blade Tip Vortices. *Journal of the American Helicopter Society*, 54, 2009.

[64] S.J. Beresh, J.F. Henfling, and R.W. Spillers. Meander of a Fin Trailing Vortex and the Origin of its Turbulence. *Experiments in Fluids*, 49:599–611, 2010.

[65] B.G. van der Wall and H. Richard. Analysis Methodology for 3C-PIV Data of Rotary Wing Vortices. *Experiments in Fluids*, 40:798–812, 2006.

[66] F. Albano, F. De Gregorio, and A. Ragni. Trailing Vortex Detection and Quantitative Evaluation of Vortex Characteristics by PIV Technique. *IEEE*, 3:31–43, 2003.

[67] P. Welch. The Use of Fast Fourier Transform for the Estimation of Power Spectra: A Method Based on Time Averaging Over Short, Modified Periodograms. *IEEE Transactions on Audio and Electroacoustics*, 15(2):70–73, 1967.

[68] M. Engel. *A Wind Tunnel Investgation of a Wing-Tip Trailing Vortex*. PhD thesis, Virginia Polytechnic Institute, 1995.

[69] S.C.C. Bailey, S. Tavoularis, and B.H.K. Lee. Effects of Free-Stream Turbulence on Wing-Tip Vortex Formation and Near Field. *Journal of Aircraft*, 43(5):1282–1291, 2006. ISSN 0021-8669.

[70] P.I. Singh and M.S. Uberoi. Experiments on Vortex Stability. *The Physics of Fluids*, 19(12), 1976. ISSN 00319171.

[71] W.R.C. Phillips and J.A.H. Graham. Reynolds Stress Measurements in a Turbulent Trailing Vortex. *Journal of Fluid Mechanics*, 147:353–371, 1984.

[72] D.S. Dosanjh, E.P. Gasparek, and S. Eskinazi. Decay of a Viscous Trailing Vortex. *The Aeronautical Journal*, 13(2):167–188, 1962.

[73] K. Yang and S. Xu. Wing Tip Vortex Structure Behind an Airfoil with Flaps at the Tip. *Science China: Physics, Mechanics and Astronomy*, 54(4):743–747, 2011.

[74] R. Narasimha and K.R. Sreenivasan. Laminarization of Fluid Flows. *Advances in Applied Mechanics*, 19:221–309, 1979.

[75] P.B. Martin and J.G. Leishman. Trailing Vortex Measurements in the Wake of a Hovering Rotor Blade With Various Tip Shapes. In *58th Annual Forum of the AHS International*, pages 2058–2080, Montréal, Canada, 2002.

[76] P.B. Martin, G.J. Pugliese, and J.G Leishman. High Resolution Trailing Vortex Measurements in the Wake of a Hovering Rotor. *Journal of the American Helicopter Society*, 48(1):39–52, 2003.

[77] O. Zeman. The Persistence of Trailing Vortices: A Modeling Study. *Physics of Fluids*, 7(1): 135–143, 1995.

[78] AJ. Cotel and R.E. Breidenthal. Turbulence Inside a Vortex. *Physics of Fluids*, 11(10):3026–3029, 1999.

[79] M. Giuni. *Formation and Early Development of Wingtip Vortices*. PhD thesis, University of Glasgow, 2013.

[80] P. Bradshaw. The Analogy Between Streamline Curvation and Buoyancy in Turbulent Shear Flow. *Journal of Fluid Mechanics*, 36(1):177–191, 1969.

[81] AJ. Cotel. Turbulence Inside a Vortex: Take Two. *Physics of Fluids*, 14(8):2933–2934, 2002.

[82] A.J. Cotel, J. A. Gjestvang, N.N. Ramkhelawan, and R.E. Breidenthal. Laboratory Experiments of a Jet Impinging on a Stratified Interface. *Experiments in Fluids*, 23:155–160, 1997. ISSN 0723-4864.

[83] M.J. Churchfield and G.A. Blaisdell. Numerical Simulations of a Wingtip Vortex in the Near Field. *Journal of Aircraft*, 46(1):230–243, 2009. ISSN 0021-8669.

[84] M.J. Churchfield and G.A. Blaisdell. Reynolds Stress Relaxation Turbulence Modeling Applied to a Wingtip Vortex Flow. *AIAA Journal*, 51(11), 2013.

[85] C. Breitsamter and A. Allen. Transport Aircraft Wake Influenced by a Large Winglet and Winglet Flaps. *Journal of Aircraft*, 46(1):175–188, 2009.

List of Figures

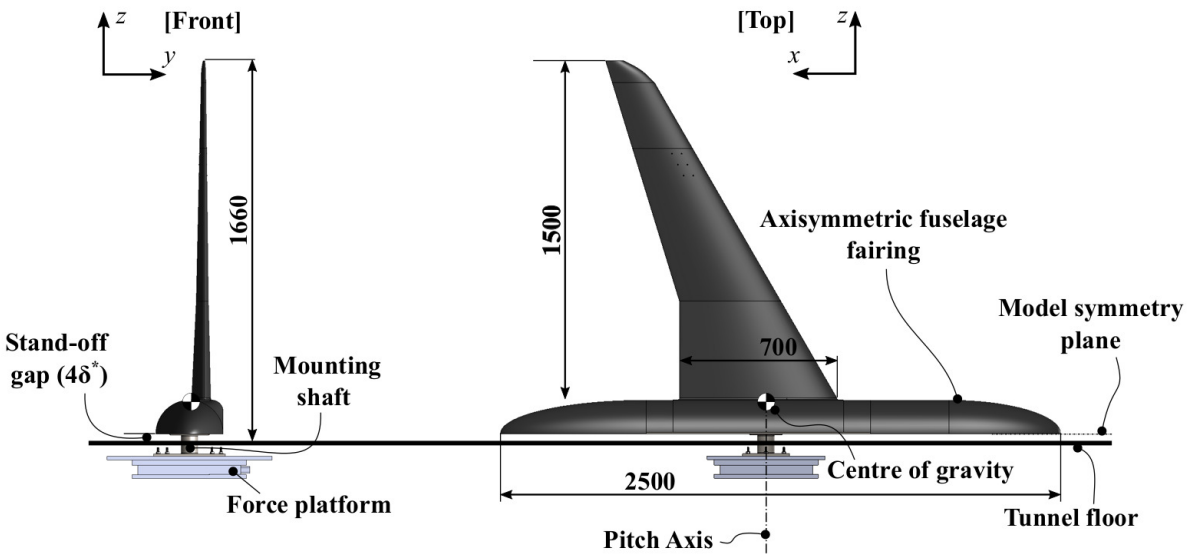

FIG. 1: Semi-span model schematic diagram; dimensions are in $[mm]$.

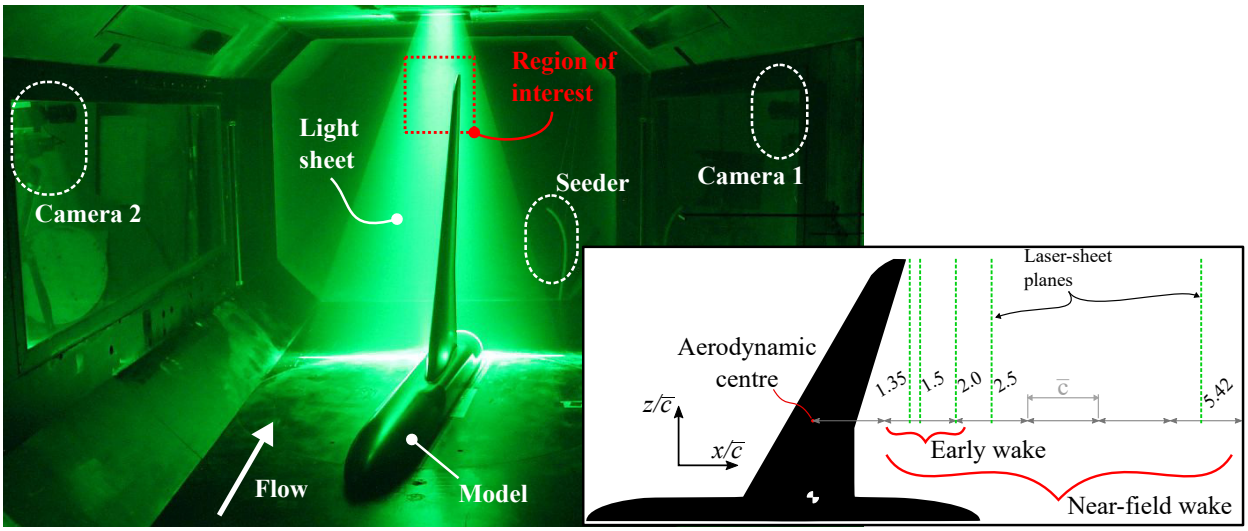

FIG. 2: sPIV experimental set up with laser sheet plane locations indicated as $x/\bar{c} = 1.35$, 1.5, 2, 2.5, and 5.418.

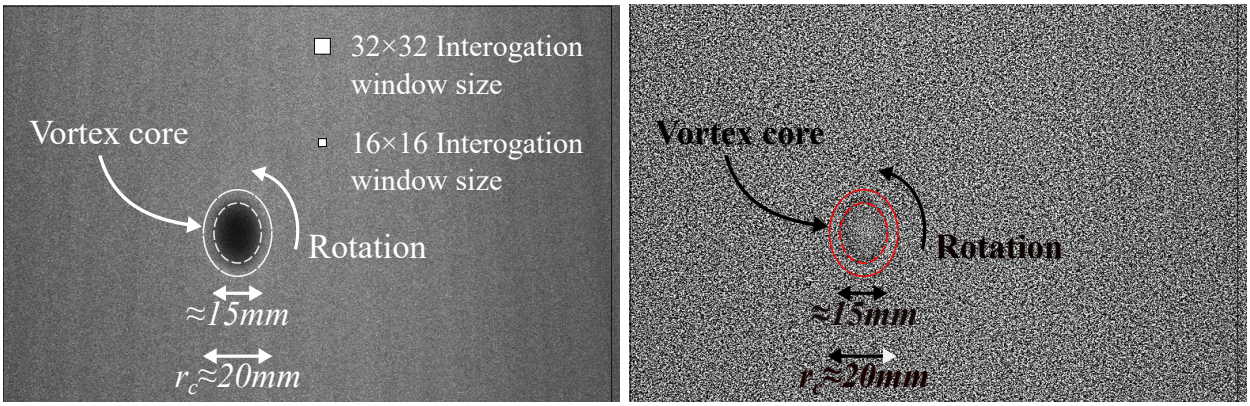

(a) (b)

FIG. 3: Instantaneous seeding distribution at $x/\bar{c} = 2.5$ for $\alpha = 8°$ from starboard camera. (a) Raw instantaneous image; and (b) Particle intensity normalisation filter applied to Figure 3(a).

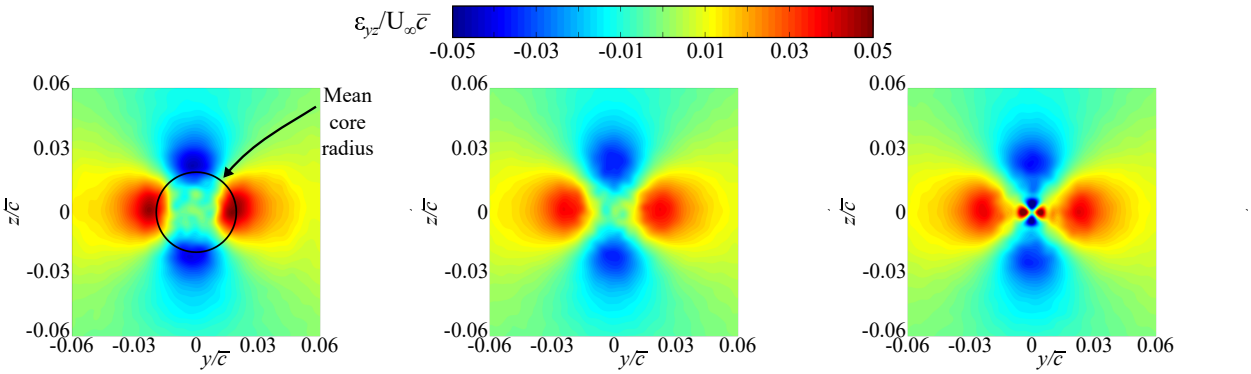

(a) (b) (c)

FIG. 4: Normalised shear strain rate, $\varepsilon_{yz}/U_\infty\bar{c}$, for alternative centering methods at $x/\bar{c} = 2.5$ and $\alpha = 8°$. (a) Simple average; (b) Zero in-plane velocity; and (c) Peak streamwise helicity.

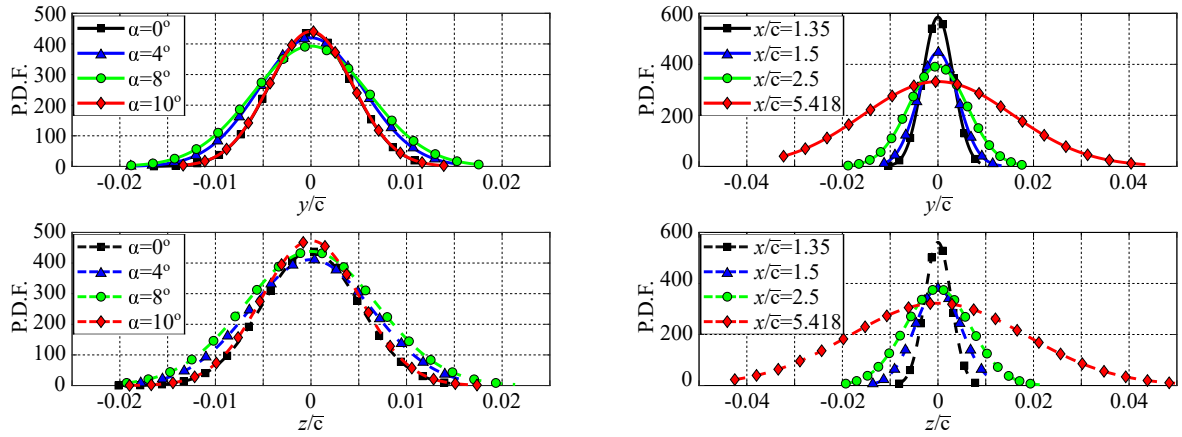

(a) (b)

FIG. 5: Probability density functions (PDF) of the vortex wander amplitudes recorded using the helicity centering method. (a) Varying α at constant downstream station $x/\bar{c} = 2.5$; and (b) Varying $x/\bar{c}$ at $\alpha = 8°$.

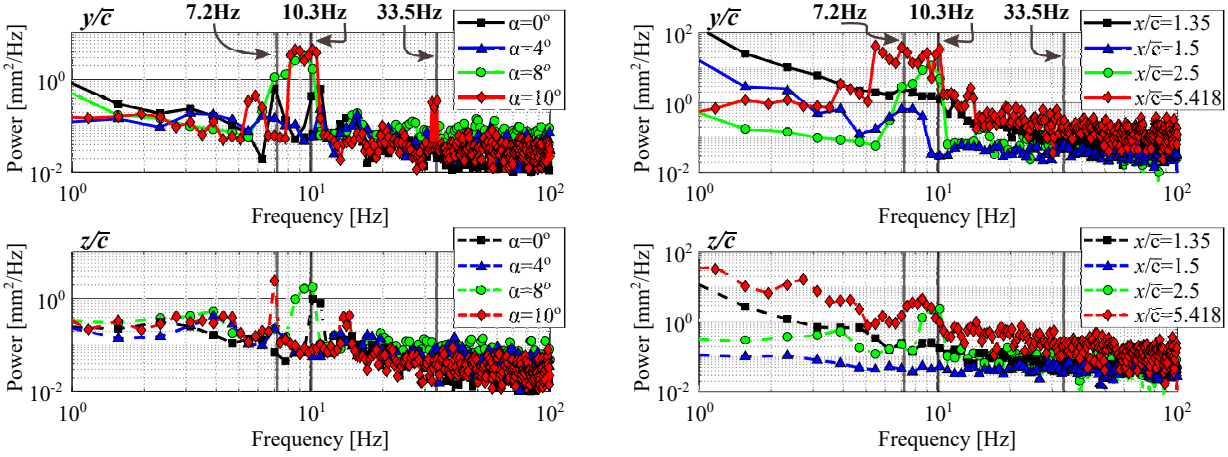

(a) (b)

FIG. 6: Spectra of the vortex wander amplitudes, in the $y/\bar{c}$ and $z/\bar{c}$ axes, recorded using the helicity centering method. (a) Varying α at constant downstream station $x/\bar{c} = 2.5$; and (b) Varying $x/\bar{c}$ at $\alpha = 8°$.

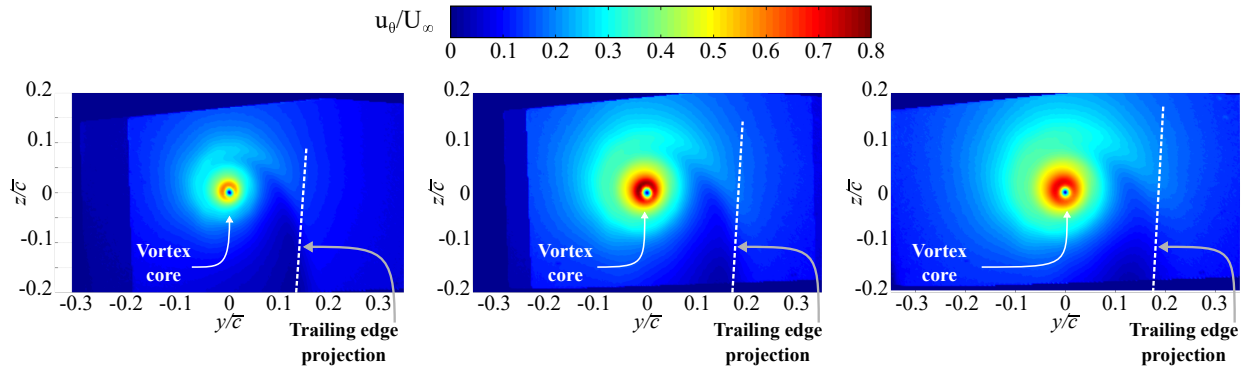

(a) (b) (c)

FIG. 7: Wing trailing vortex tangential velocity contours at $x/\bar{c} = 2.5$ for: (a) $\alpha = 4°$; (b) $\alpha = 8°$; and (c) $\alpha = 10°$.

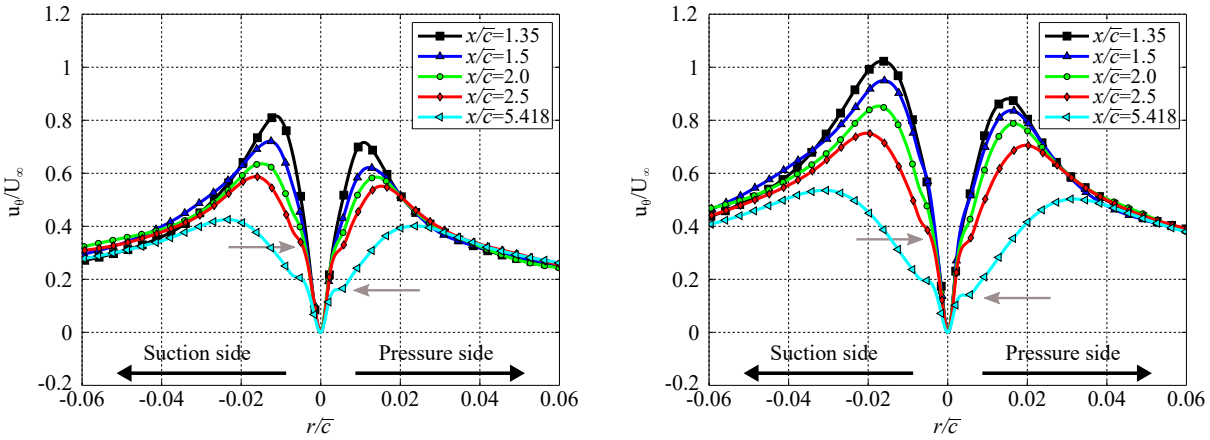

(a) (b)

FIG. 8: Mean tangential velocity development as a function of $x/\bar{c}$ plane for: (a) $\alpha = 4°$; and (b) $\alpha = 8°$.

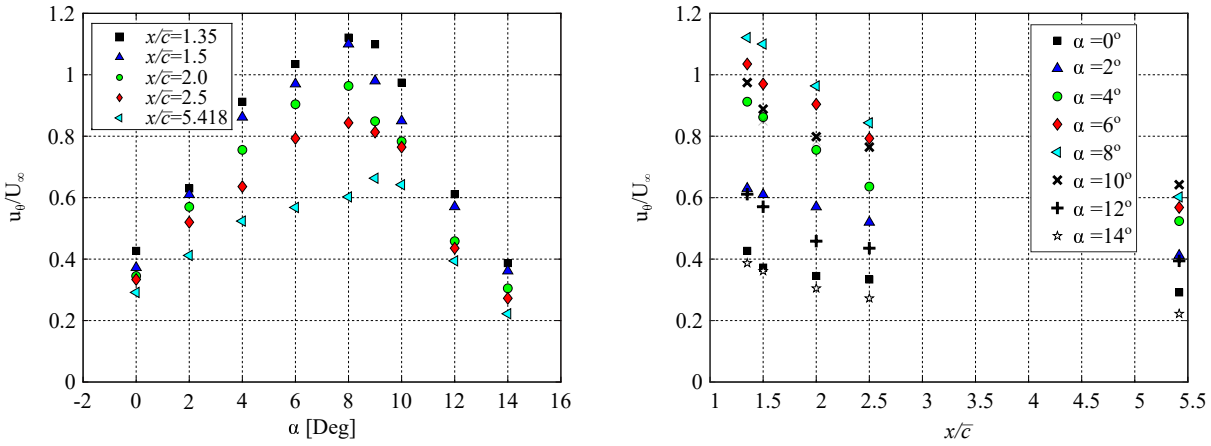

(a) (b)

FIG. 9: Peak tangential velocity at different $x/\bar{c}$ planes as a function of α. (a) Peak swirl Vs. α; and (b) Peak swirl Vs. $x/\bar{c}$.

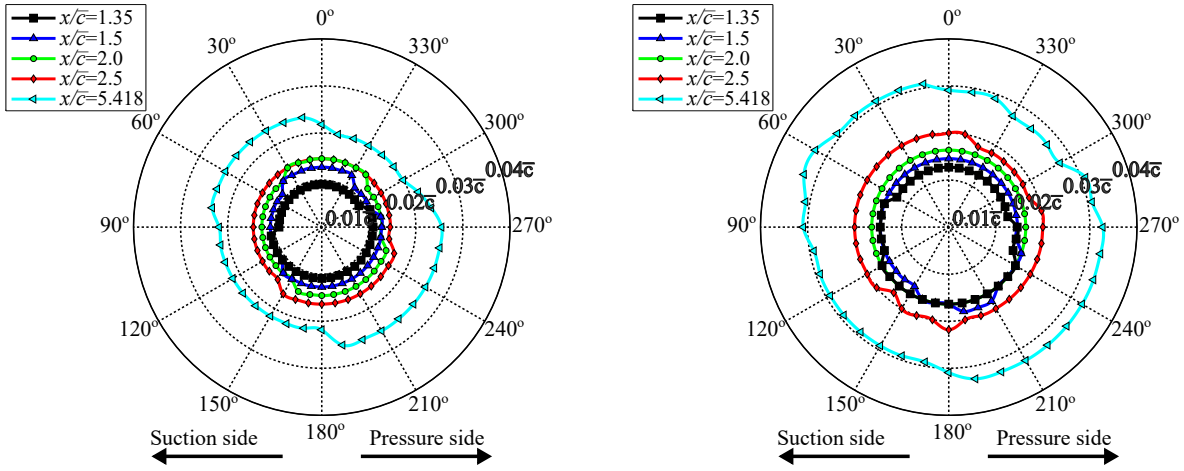

(a) (b)

FIG. 10: Polar plots illustrating the development of the time-averaged vortex core shape as a function of $x/\bar{c}$ plane for: (a) $\alpha = 4°$; and (b) $\alpha = 8°$.

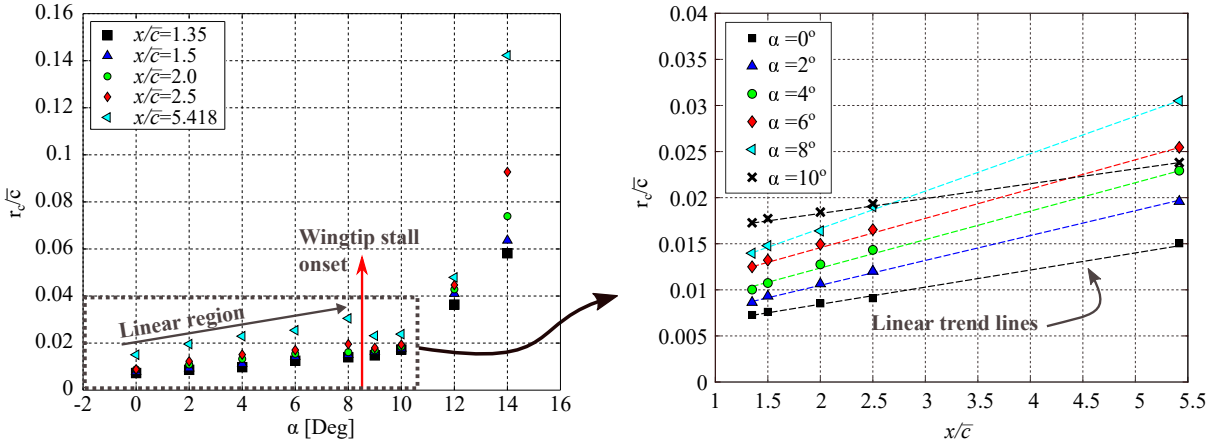

(a) (b)

FIG. 11: Mean vortex core radius for different $x/\bar{c}$ planes as a function of α. (a) Mean radius Vs. α; and (b) Mean radius Vs. $x/\bar{c}$.

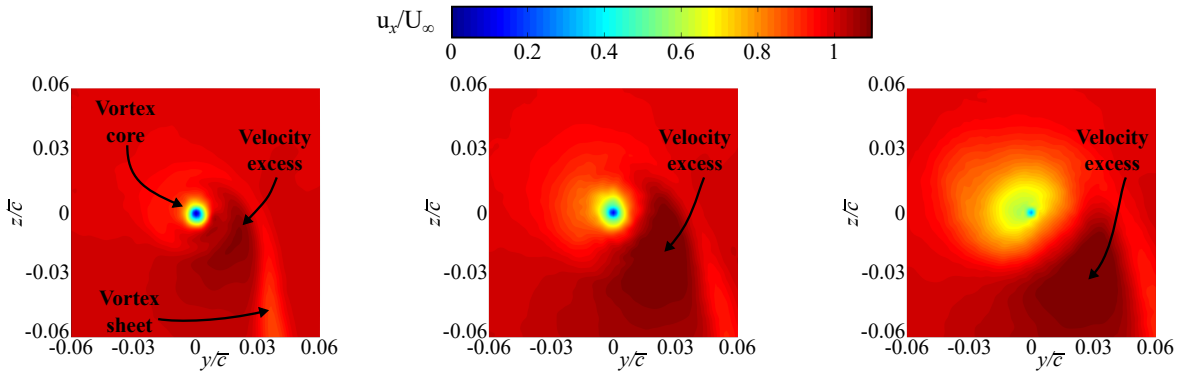

(a) (b) (c)

FIG. 12: Wing trailing vortex axial velocity contours at $x/\bar{c} = 2.5$ for: (a) $\alpha = 4°$; (b) $\alpha = 8°$; and (c) $\alpha = 10°$.

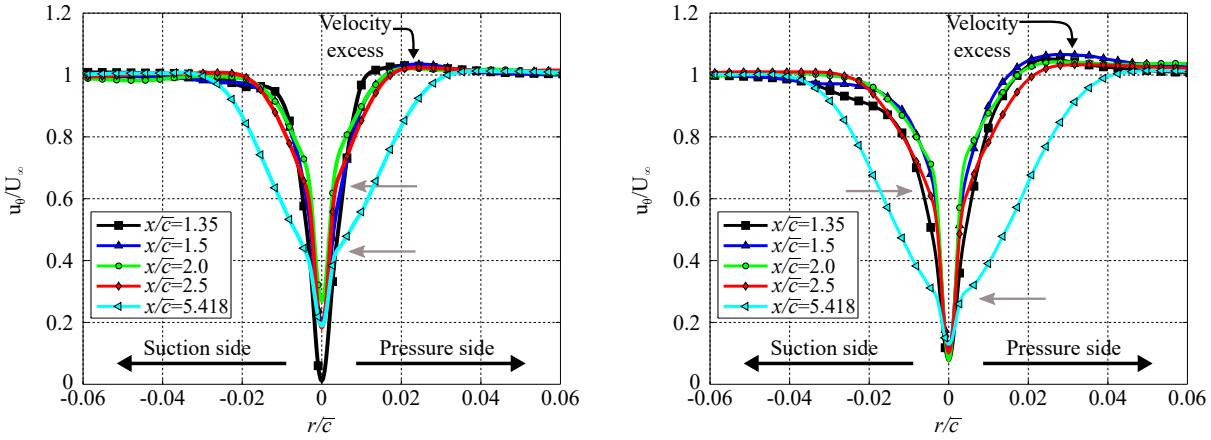

(a) (b)

FIG. 13: Axial velocity development as a function of $x/\bar{c}$ plane for: (a) $\alpha = 4°$; and (b) $\alpha = 8°$.

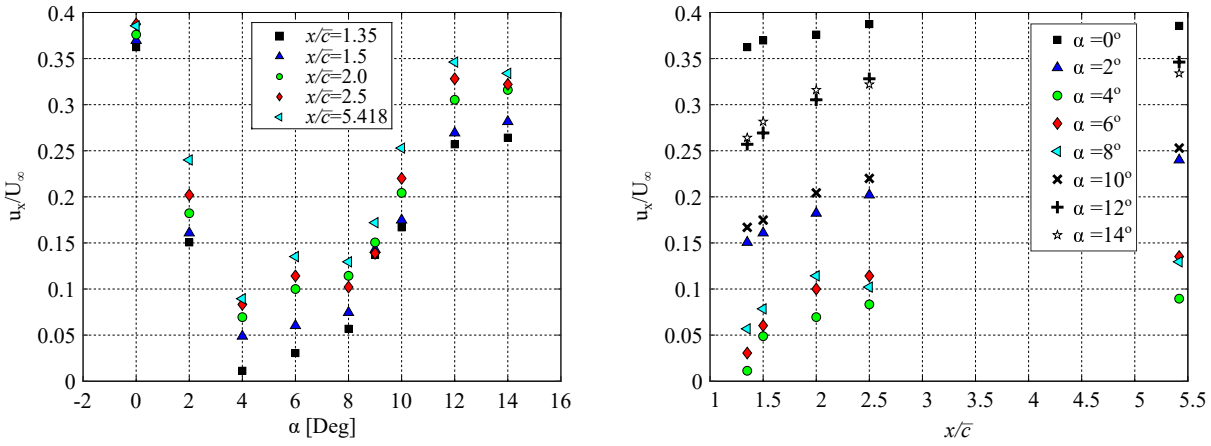

(a) (b)

FIG. 14: Peak axial velocity for different $x/\bar{c}$ planes as a function of α. (a) Peak u_x Vs. α; and (b) Peak u_x Vs. $x/\bar{c}$.

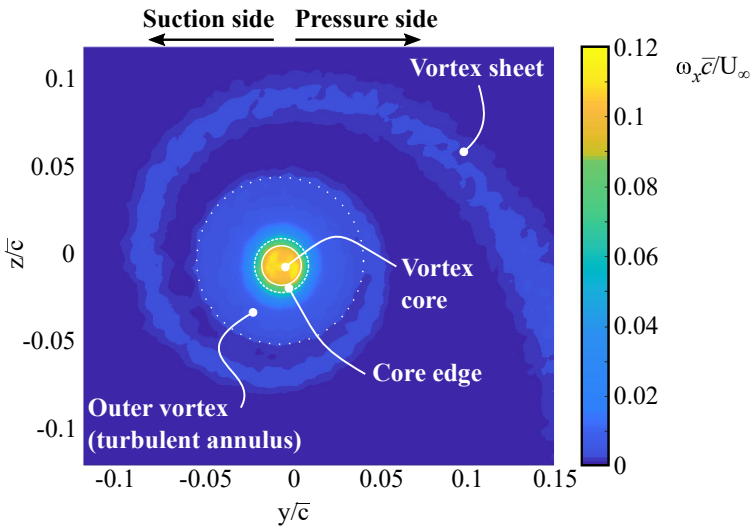

FIG. 15: Vorticity distribution illustrating the vortex sheet roll-up and merging to form trailing vortex for $x/\bar{c} = 2.5$, with $\alpha = 8°$. The scaling here has been determined to accentuate vortex features.

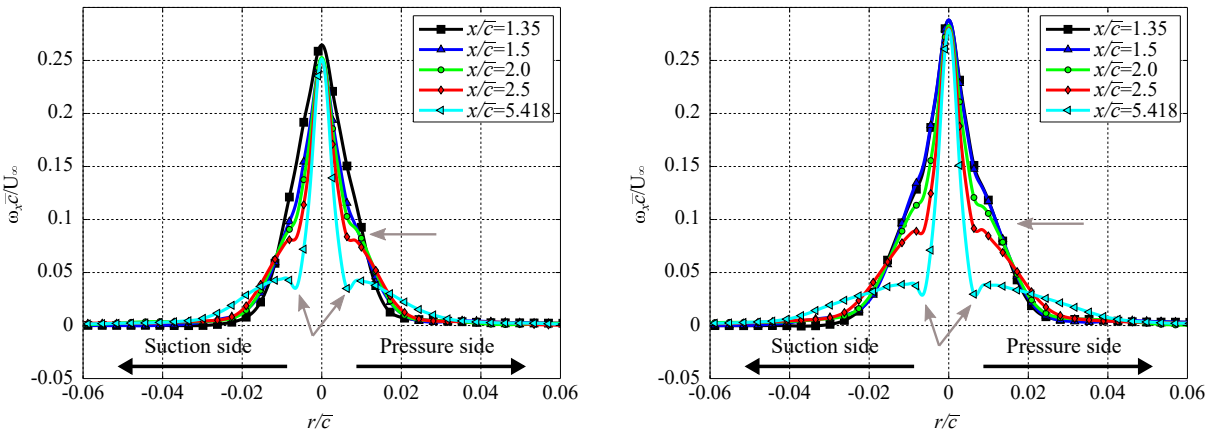

(a) (b)

FIG. 16: Vorticity development as a function of $x/\bar{c}$ plane for: (a) $\alpha = 4°$; and (b) $\alpha = 8°$.

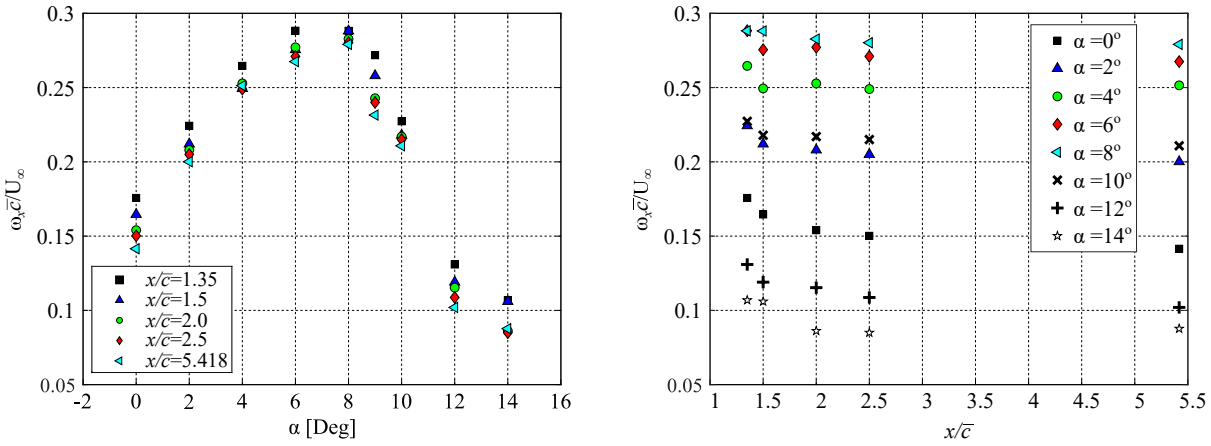

(a) (b)

FIG. 17: Peak vorticity for different $x/\bar{c}$ planes as a function of α. (a) Peak vorticity Vs. α; and (b) Peak vorticity Vs. $x/\bar{c}$.

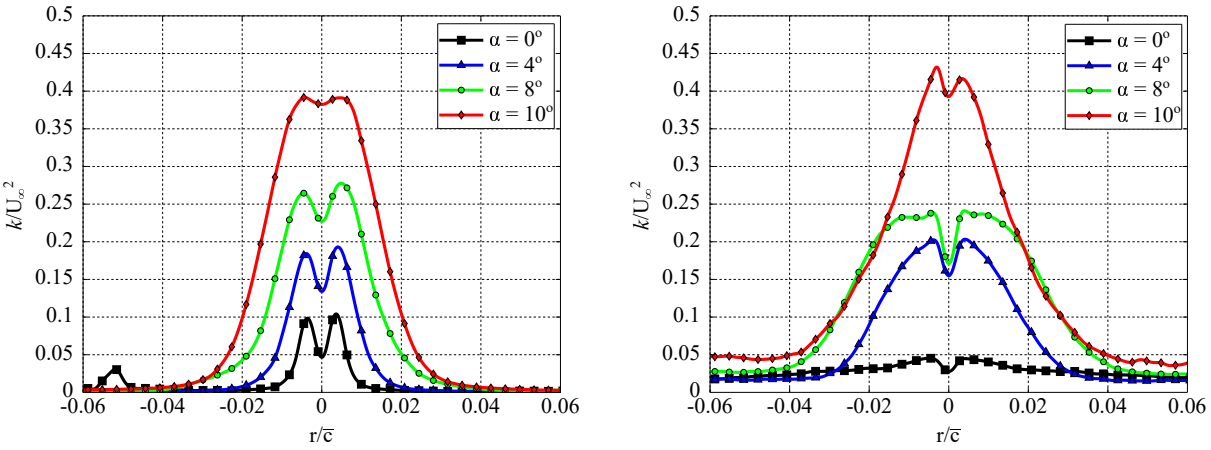

(a) (b)

FIG. 18: Turbulent kinetic energy through vortex core vertical plane (along $z/\bar{c}$ at $y/\bar{c} = 0$ for $\alpha = 0°$, 4°, 8°, and 10° at downstream station: (a) $x/\bar{c} = 1.35$; and (b) $x/\bar{c} = 5.418$.

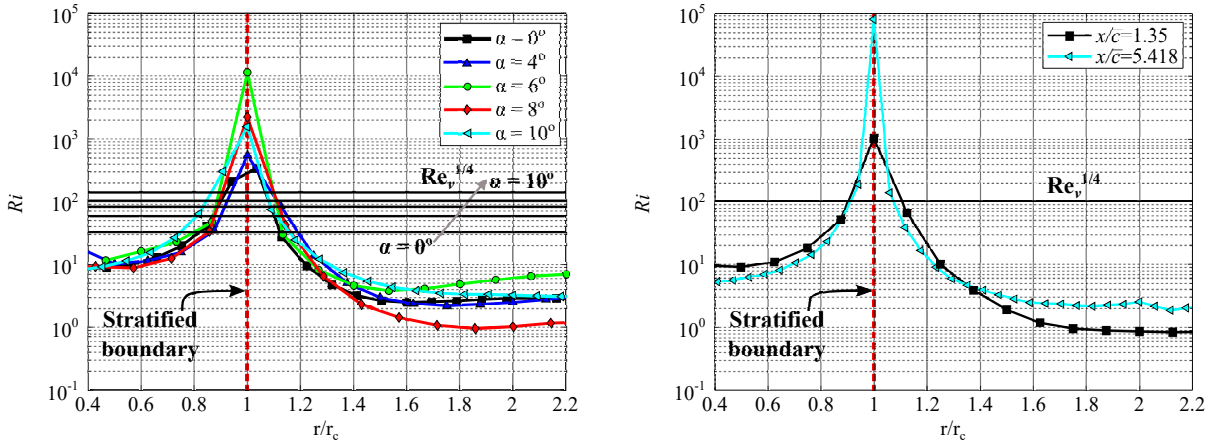

(a) (b)

FIG. 19: Richardson number as a function of distance from the vortex core centre for: (a) $\alpha = 0°$, 4°, 6°, 8°, and 10° at $x/\bar{c} = 2.5$; and (b) $\alpha = 8°$ at $x/\bar{c} = 1.35$ and 5.418.

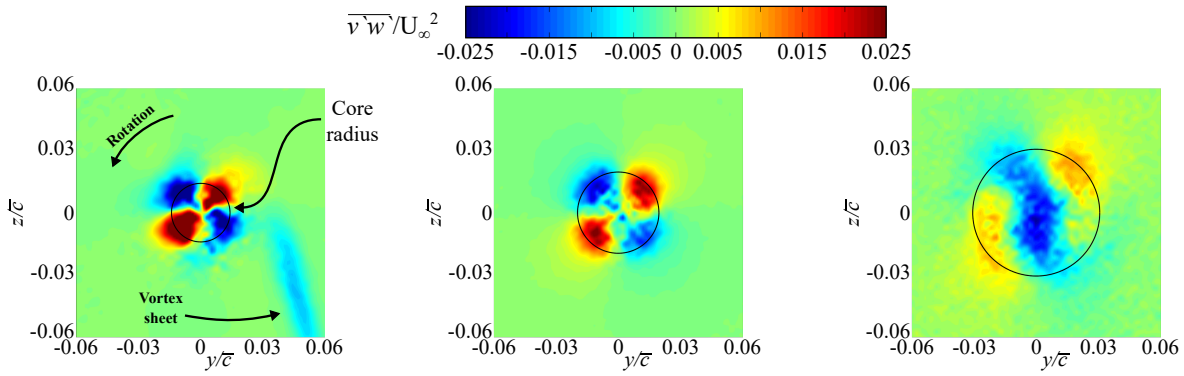

(a) (b) (c)

FIG. 20: Streamwise development of the in-plane Reynolds shear stresses ($\overline{v'w'}/U_\infty^2$) for $\alpha = 8°$ at: (a) $x/\bar{c} = 1.35$; (b) $x/\bar{c} = 2.5$; and (c) $x/\bar{c} = 5.418$.

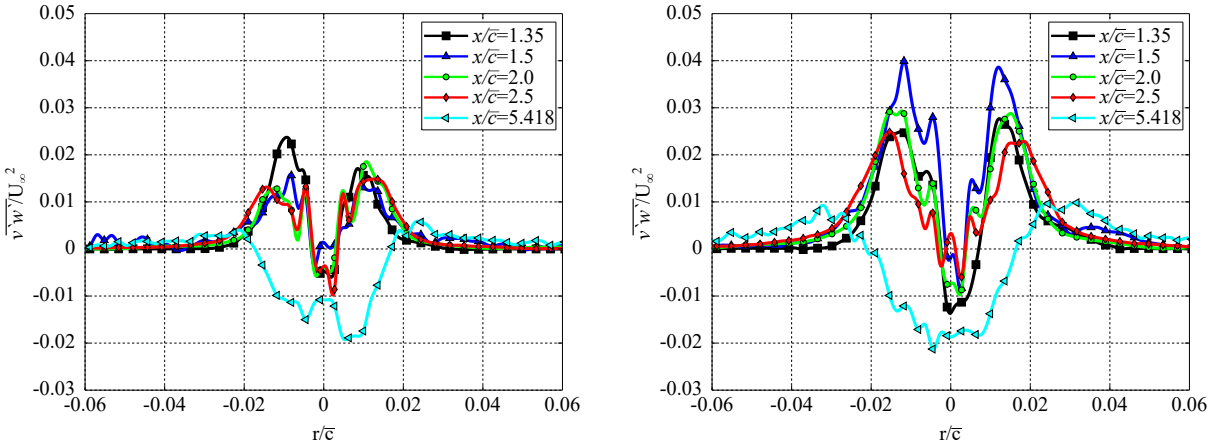

FIG. 21: Streamwise development of the in-plane Reynolds shear stresses ($\overline{v'w'}/U_\infty^2$) for: (a) $\alpha = 4°$; and (b) $\alpha = 8°$. *Note: data slices taken at* 135° *through the positive lobes illustrated in Figure 20.*

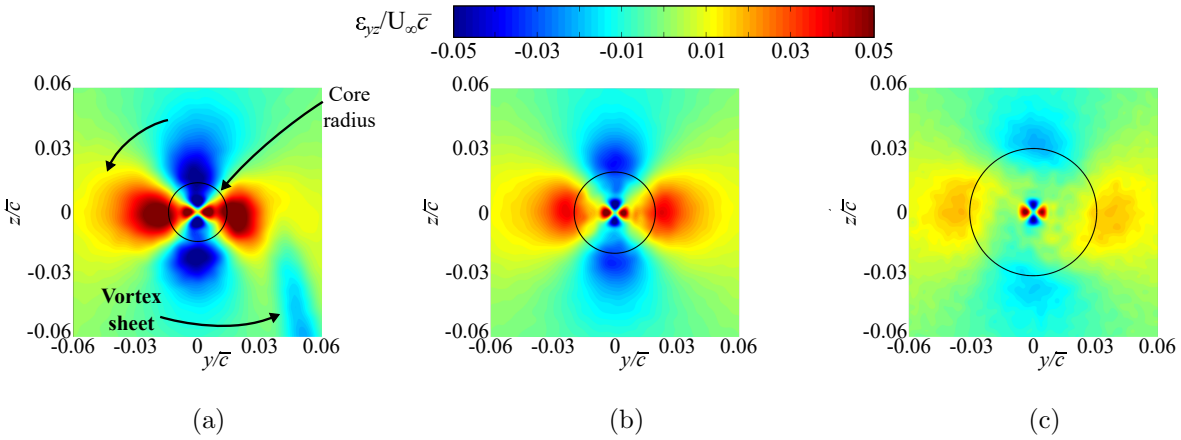

FIG. 22: Streamwise development of the shear strain rates ($\varepsilon_{yz}/U_\infty\bar{c}$) for $\alpha = 8°$ at: (a) $x/\bar{c} = 1.35$; (b) $x/\bar{c} = 2.5$; and (c) $x/\bar{c} = 5.418$.

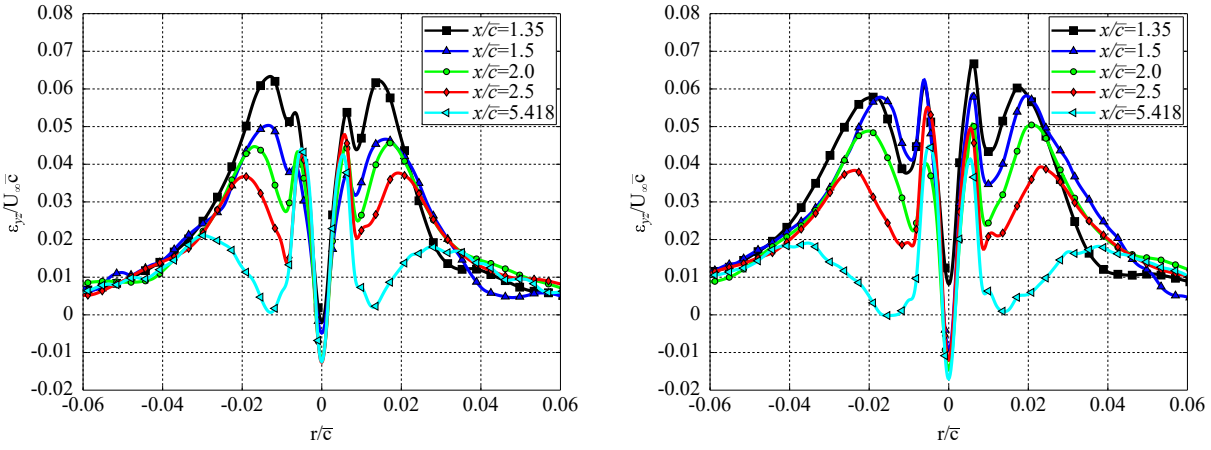

FIG. 23: Streamwise development of the shear strain rates ($\varepsilon_{yz}/U_\infty\bar{c}$) for: (a) $\alpha = 4°$; and (b) $\alpha = 8°$. *Note: data slices taken along* $y/\bar{c}$ *at* $z/\bar{c} = 0$ *for data presented in Figure 22.*

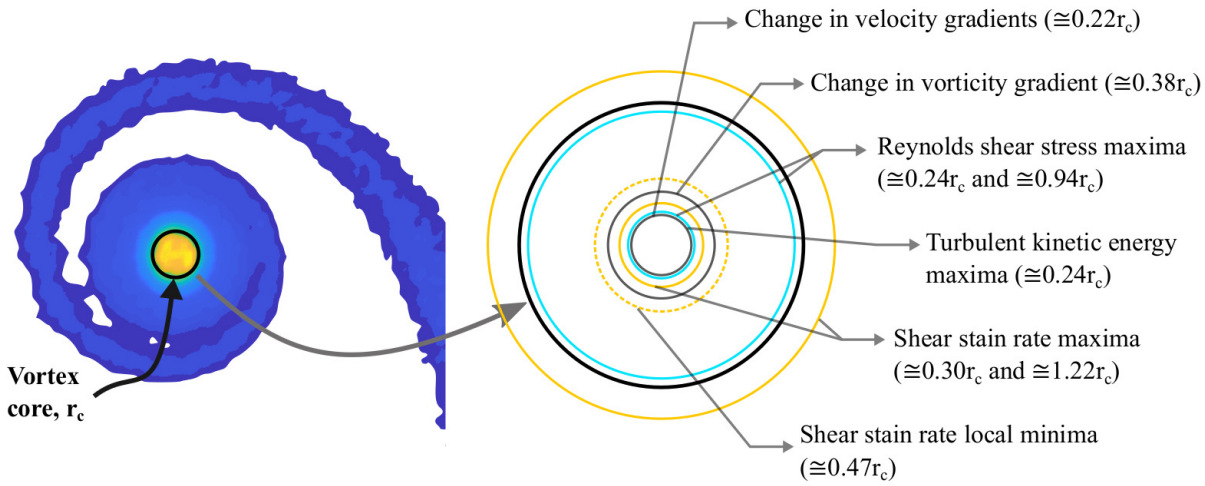

FIG. 24: Schematic of the trailing vortex core structure.

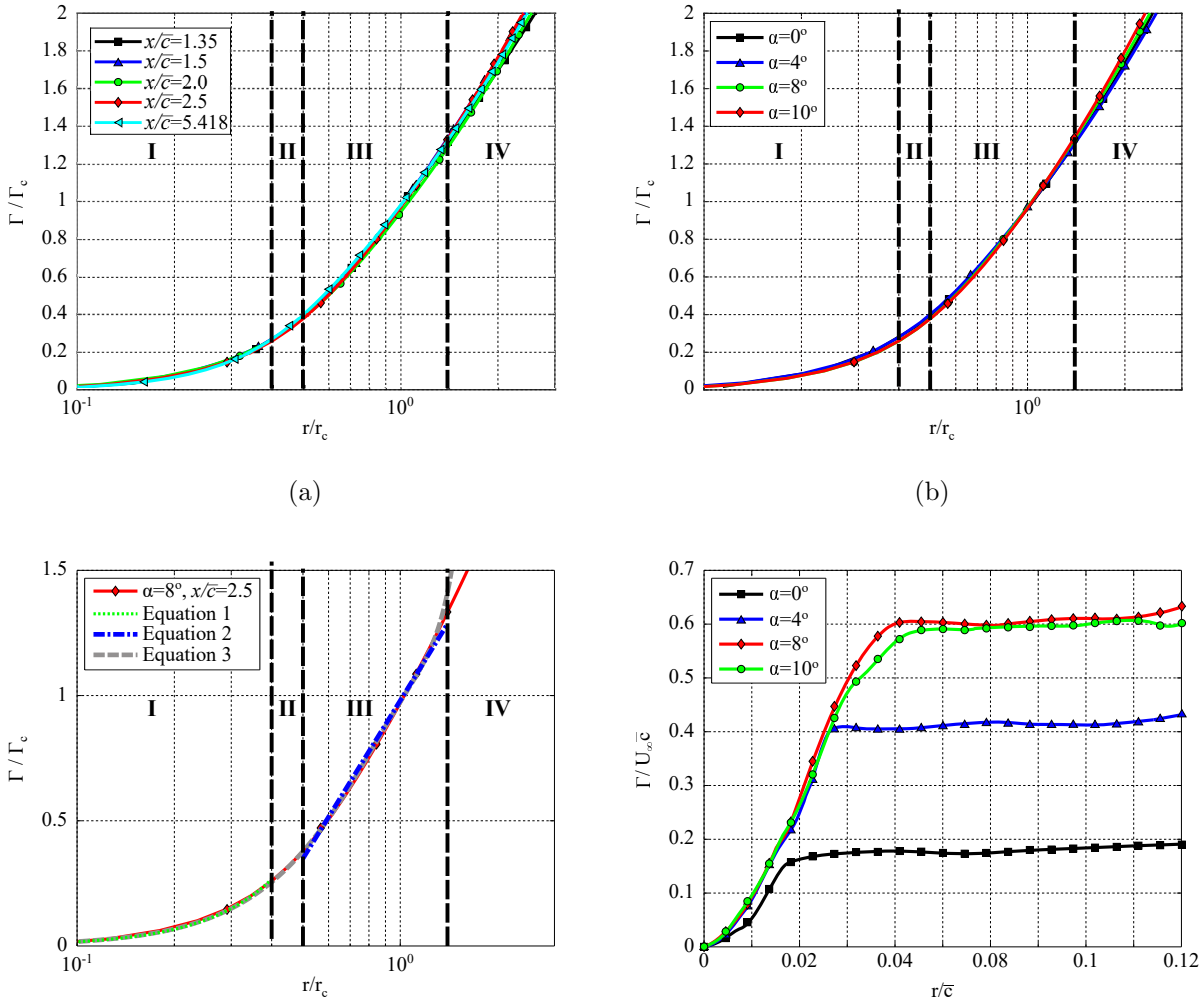

FIG. 25: Radial distribution of circulation: **I**, inner-core region; **II**, buffer region; **III**, logarithmic region; and **IV**, outer region. (a) Variation with $x/\overline{c}$; (b) Variation with α; (c) Universal circulation profile; and (d) Radial circulation distribution at $x/\overline{c} = 2.5$.

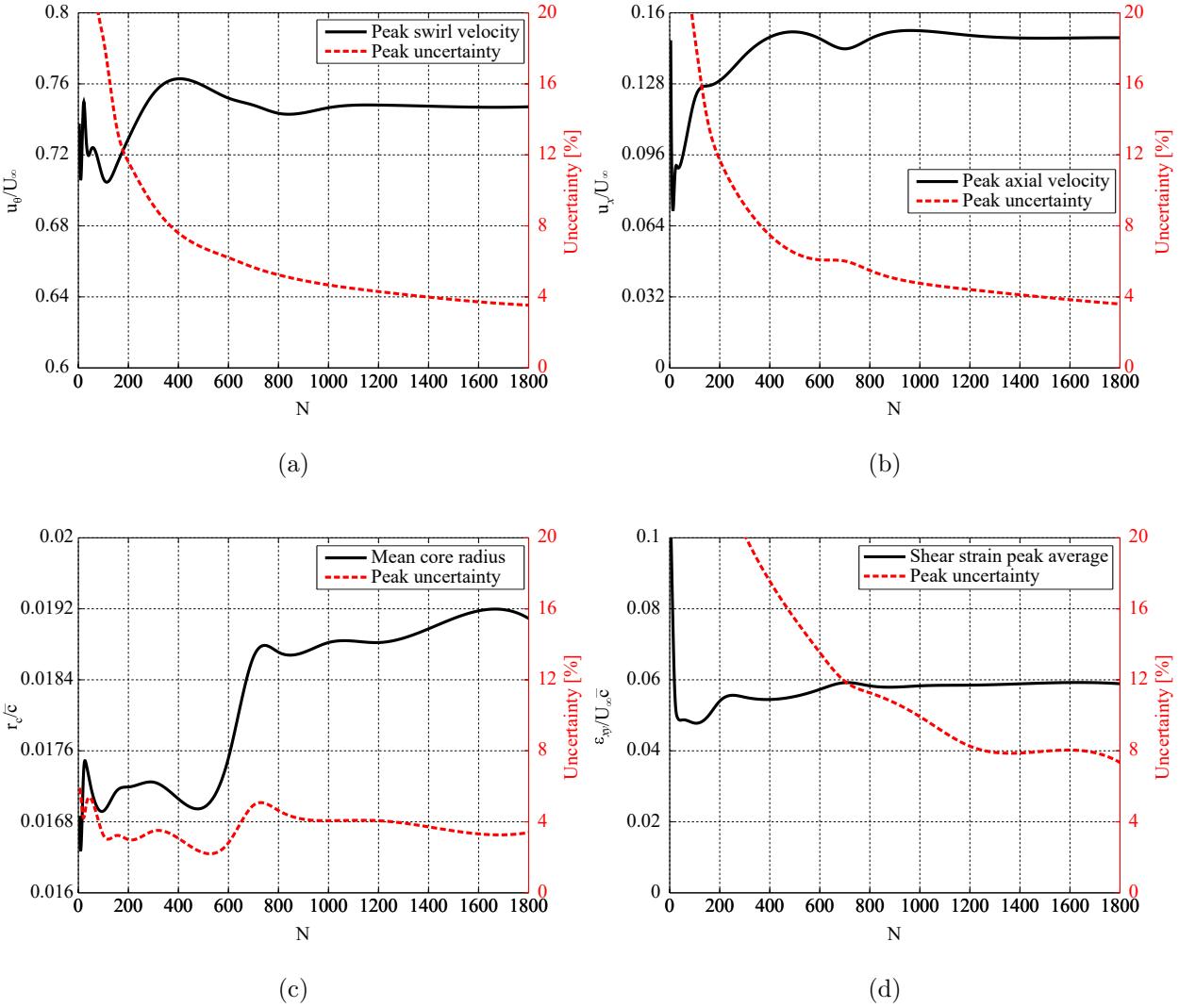

FIG. 26: Convergence analysis of vortex properties showing peak uncertainty within field of view (typically found within the vortex core) for a confidence level of 95% for $\alpha = 8°$ at $x/\bar{c} = 2.5$. (a) Tangential velocity; (b) Axial velocity; (c) Vortex core radius; and (d) Shear strain rate.